nature immunology

Article

https://doi.org/10.1038/s41590-023-01691-y

GIMAP5 deficiency reveals a mammalian ceramide-driven longevity assurance pathway

Received: 19 April 2023

Accepted: 26 October 2023

Published online: 3 January 2024

Check for updates

A list of authors and their affiliations appears at the end of the paper

Preserving cells in a functional, non-senescent state is a major goal for extending human healthspans. Model organisms reveal that longevity and senescence are genetically controlled, but how genes control longevity in different mammalian tissues is unknown. Here, we report a new human genetic disease that causes cell senescence, liver and immune dysfunction, and early mortality that results from deficiency of GIMAP5, an evolutionarily conserved GTPase selectively expressed in lymphocytes and endothelial cells. We show that GIMAP5 restricts the pathological accumulation of long-chain ceramides (CERs), thereby regulating longevity. GIMAP5 controls CER abundance by interacting with protein kinase CK2 (CK2), attenuating its ability to activate CER synthases. Inhibition of CK2 and CER synthase rescues GIMAP5-deficient T cells by preventing CER overaccumulation and cell deterioration. Thus, GIMAP5 controls longevity assurance pathways crucial for immune function and healthspan in mammals.

Longevity assurance (LASS) pathways, which ensure cell vitality and proliferation, were first defined to be under genetic control in *Saccharomyces cerevisiae*, where regulation of cell divisions, rather than chronological age, define lifespan[1]. Notably, the deletion of a gene called longevity assurance gene 1 (*LAG1*), which is one of a group of LASS genes that are conserved from yeast to humans encoding CER synthases (CERS), substantially increased lifespan in yeast[2,3]; however, the molecular mechanisms specifically regulating cellular longevity assurance pathways in mammals, especially humans, are poorly understood. CERs are structural components of cell membranes as well as second messengers for stress or receptor signaling[4,5]. Low, transient CER levels can transduce signals from cell surface receptors, whereas high sustained levels can cause cellular disruption and degeneration[5,6]. In the immune system, lymphocyte longevity is crucial for protective immunity, vaccine efficacy and successful immunotherapies. T cell receptor (TCR) signaling is known to induce a transient CER burst, but the effects of CER overaccumulation and how LASS pathways are controlled are unknown[7].

In vertebrates, *GIMAP5* is a member of a conserved family of eight clustered G protein genes, in humans on chromosome 7q36, encoding the GTPase of immunity-associated proteins (GIMAPs; also known as immune-associated nucleotide-binding proteins). These have especially high expression in lymphocytes and non-lymphoid endothelial cells (ECs)[8,9]. GIMAPs localize to different cell compartments and are structurally related to dynamin/septins, which are activated by nucleotide-dependent dimerization[10–12].

GIMAP5 is perhaps the best-known GIMAP due to the prominent immunoregulatory role first observed in the classic biobreeding (BB) rat model of type 1 diabetes[8,13]. BB rats harbor a homozygous frameshift mutation that eliminates GIMAP5 protein expression leading to severe T cell lymphopenia, a deficit of regulatory T cells and type I diabetes or colitis, depending on the genetic background[8,13]. Mice deficient for Gimap5, for example, the ethyl nitrosourea-generated *sphinx* mouse (named for its enigmatic characteristics) or those with genetically engineered deficiencies, also have progressive T and natural killer (NK) cell lymphopenia[14–16]. Together these results suggest a specific role for GIMAP5 in regulating lymphocyte youthfulness and lifespan. Various functions of GIMAP5, such as regulation of Bcl-2 family proteins, nuclear factor (NF)-κB, mTOR, lysosomal calcium control and c-Myc stabilization by glycogen synthetase kinase have been described,

e-mail: lenardo@nih.gov

https://doi.org/10.1038/s41590-023-01691-y

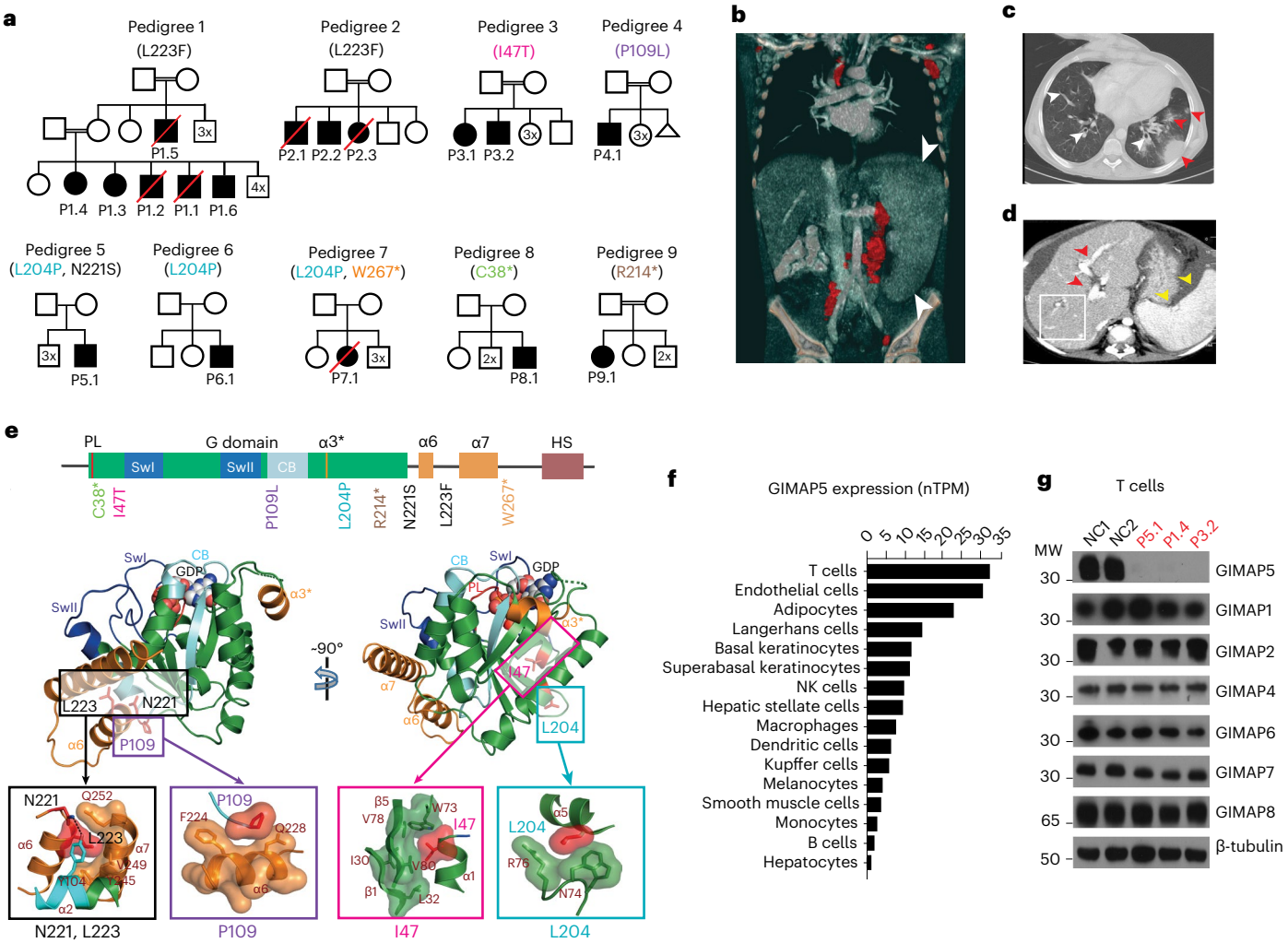


Fig. 1 | New human immune disease caused by loss-of-function *GIMAP5* mutations. a, Patient (P) pedigrees showing GIMAP5 amino acid substitutions. Asterisk (*) indicates stop-gain; red strikethrough, deceased; double line, consanguinity. Same-sex siblings enumerated 2x, etc. **b**, Computerized tomography (CT) scan of P5.1. Enlarged lymph nodes as highlighted in red and enlarged spleen indicated by white arrowheads. **c**, P1.2 chest CT showing bronchiectasis (white arrowheads) and lung consolidation due to acute infection (red arrowheads). **d**, Abdominal CT of P4.1 showing splenomegaly (yellow arrowheads), heterogenous liver parenchyma (white box) and dilated portal vein branches (red arrowheads). **e**, GIMAP5 protein domains; GTPase domain, switch I (SwI) and switch II (SwII) (blue), the P-loop (PL) (red), the conserved box (CB) (cyan) and GIMAP-specific elements: alpha helices (α) α3*, α6 and α7 (orange) and the hydrophobic segment (HS, maroon) (top). Crystal structure of GDP-bound GIMAP5[1–276] (bottom). Boxes show amino acids mutated in patients. **f**, Summary of normalized expression (nTPM) of *GIMAP5* mRNA from different single-cell types from the Human Protein Atlas. **g**, GIMAP5 protein immunoblots of P versus normal control (NC) T cells compared to GIMAP1, 2, 4, 5, 6, 7 and 8 proteins and β-tubulin control ($n = 3$). GIMAP5 has two isoforms in human cells that are undiscernible in the overexposed blot.

but the regulatory role of GIMAP5, especially in the human immune system, is unresolved[17–21]. In humans, genome-wide association studies have uncovered single nucleotide polymorphisms in GIMAP genes linked to asthma, type 1 diabetes, systemic lupus erythematosus and Behcet's disease, and a monogenic immune dysregulation in a single case has been reported[21–24]. Also, a genetic analysis has shown that GIMAP5 critically controls liver EC differentiation and prevents portal hypertension[9]. Collectively, these findings underscore the importance of GIMAP5 in normal lymphocyte and EC physiology, but its precise molecular role within the cell has been mysterious. Here we describe biochemical abnormalities and a new mammalian GIMAP5 function in a clinical setting and specifically connect GIMAP5 to LASS pathways.

Results

New human disease from *GIMAP5* loss-of-function mutations

From our international clinical genomics research cohort, we identified 17 affected individuals in nine kindreds with *GIMAP5* loss-of-function mutations (Fig. 1a). Affected individuals suffered from splenomegaly, liver disease, lymphopenia, severe recurrent lung infections with pneumonia and bronchiectasis, thrombocytopenia, lymphadenopathy, skin diseases and lymphoma (Fig. 1b–d, Extended Data Fig. 1a, Table 1, Supplementary Tables 1 and 2 and Supplementary clinical descriptions). Six patients died: one from pulmonary embolus, two from liver failure, two from complications of SARS-CoV-2 infection and one from *Enterococcus faecium* sepsis following relapse of Hodgkin's lymphoma and hematopoietic stem cell transplantation (Fig. 1a). Longitudinal studies showed decreased absolute lymphocyte counts, immunoglobulin abnormalities and a high incidence of lymphoma (Extended Data Fig. 1b and Supplementary Tables 1 and 2). Portal hypertension was associated with liver disease findings (Fig. 1d, Extended Data Fig. 1a and Supplementary Table 1) and has been recently shown to involve liver EC abnormalities[9].

The genetic abnormalities in affected individuals were either missense or stop-gain mutations in *GIMAP5* with either bi-allelic

Table 1 | Summary of key clinical findings in GIMAP5-deficient patients

Clinical findings	Cohort
Splenomegaly	17 of 17
Liver disease	13 of 17
Lymphopenia	13 of 17
Lung findings	12 of 17
Thrombocytopenia	13 of 17
Lymphadenopathy	7 of 17
Skin disorders	8 of 17
Lymphoma	5 of 17

homozygous or compound heterozygous inheritance, causing substitutions of amino acids L223F, I47T, P109L, L204P, N221S, W267* and C38*, which are generally conserved across species and/or the GIMAP gene family and a less-conserved R214* (Fig. 1a and Extended Data Fig. 1c)[9]. Bioinformatics showed these single nucleotide variants to be rare and deleterious (Supplementary Table 3). To understand these mutations, we determined the X-ray crystallographic structure of GDP-bound GIMAP5 (amino acids 1–276; GIMAP5$^{1–276}$) with a resolution of 2.8 Å (Fig. 1e, Extended Data Fig. 1d and Supplementary Table 4). GIMAP5$^{1–276}$ adopts a typical G domain fold with a C-terminal helical extension. The structure is closely related to that of GIMAP2 and GIMAP7, but has a short helical extension resembling the former (Extended Data Fig. 1e)[11,25]. Based on their position, the patient variants likely cause major structural disturbances (Fig. 1e, small panels and supplementary descriptions). Concordantly, glutathione-*S*-transferase (GST) fusion proteins of GIMAP5$^{1–276}$ containing patient mutations showed altered thermal shift profiles consistent with reduced protein stability (Extended Data Fig. 1f).

Human *GIMAP5* messenger RNA is highly expressed in T cells, ECs and NK cells, but much less in CD14$^+$ monocytes or CD19$^+$ B cells (Fig. 1f and Extended Data Fig. 1g)[26]. Immunoblots (IBs) confirmed the high GIMAP5 protein expression in human NK and T cells, but not in B cells or monocytes (Extended Data Fig. 1g). Patients' T cells showed loss of GIMAP5 protein but had normal protein levels of GIMAP1, 2, 4, 6, 7 and 8, confirming that the genetic variants cause selective GIMAP5 protein instability (Fig. 1g and Extended Data Fig. 1i). *GIMAP5* mRNA levels were generally normal in patient T cells, except P8.1 who has a premature stop codon mutation at amino acid 38 leading to reduced mRNA by nonsense-mediated decay (Extended Data Fig. 1j). Thus, loss-of-function *GIMAP5* mutations lead to human diseases characterized by lymphopenia, recurrent infections and liver disease.

GIMAP5 deficiency induces senescence in human lymphocytes

We analyzed patient lymphocytes using 38 time-of-flight mass cytometry (CyTOF) markers and observed selectively depleted naive CD4$^+$ and CD8$^+$ T cells and central memory (T_{CM}) CD4$^+$ T cells but increased effector memory (T_{EM}) CD4$^+$ and CD8$^+$ T cells (Extended Data Fig. 2a, Supplementary Table 5, 6)[27]. We confirmed significantly decreased CD45RA$^+$CCR7$^+$ naive CD4$^+$ and CD8$^+$ T cells and increased CD45RA$^-$CCR7$^-$ T_{EM} cells in patient samples; naive CD4$^+$ and CD8$^+$ T cells were reduced to half or less compared to age-matched controls by flow cytometry (Fig. 2a and Extended Data Fig. 2b[28]). These data suggested persistent overactivation, so we analyzed the CD57 senescence marker and found it increased on the patients' CD8$^+$ T_{EM}, T_{CM}, terminally differentiated effector memory (T_{EMRA}) and γδ T cells but to a lesser degree on CD4$^+$ T cells by flow cytometry and CyTOF (Fig. 2b and Extended Data Fig. 2c,d).

We further verified T cell senescence by finding increased senescence-associated-β-galactosidase (SA-β-gal) activity and elevated surface KLRG and reduced CD27 and CD28 in patient cells (Fig. 2c and Extended Data Fig. 2e–h). We found that PD-1 was only modestly elevated and there was marked shortening of telomeres (less than the first percentile) in some samples suggesting that the patient T cells may be in a senescent state different from exhaustion[29] (Extended Data Fig. 2i,j). Consistent with reduced naive cells and increased senescent cells, we observed reduced CD25 and CD69 expression and proliferation after TCR stimulation of patient T cells directly ex vivo (Extended Data Fig. 2k–m and Fig. 2d). We also examined the biochemical machinery of senescence and found that intracellular staining for p21, p53 and p16 was elevated for patient T cells (Fig. 2e). Patient plasma also had a senescence-associated secretory phenotype with increased interleukin (IL)-6 and IL-8 (Fig. 2f).

We then performed acute CRISPR/Cas9 knockout (KO) of *GIMAP5* (GIMAP5^{CrKO}) or a non-targeting control (Ctrl) in purified naive healthy human CD8$^+$ T cells to explore the effects of acute loss of GIMAP5 function (Fig. 2g)[30]. GIMAP5^{CrKO} T cells had reduced long-term proliferation and increased cell cycle inhibitors, p21, p53 and p16 (Fig. 2h,i). We did not find reduced c-Myc (Fig. 2i) as previously reported, but did observe a G2/M phase cell cycle arrest for GIMAP5^{CrKO} T cells, which p21 causes in non-canonical senescence (Extended Data Fig. 2n)[21,31]. Viability was modestly reduced in GIMAP5^{CrKO} T cells and there was no difference in the expression of the activation markers, CD25 and CD69 in GIMAP5^{CrKO} T cells after TCR stimulation (Extended Data Fig. 2o,p). In summary, acute *GIMAP5* KO in human T cells induces senescence and cell cycle arrest like the patient T cell phenotype, verifying that *GIMAP5* gene deficiency accounts for disease in our patient cohort.

Gimap5 deficiency induces senescence in mice

We next explored whether Gimap5 deficiency also drives cell senescence in mice using the *sphinx* mouse strain (*Gimap5$^{sph/sph}$*) that harbors a *Gimap5* point mutation leading to protein instability and loss[15]. In littermate control mice, Gimap5 was expressed in the spleen and liver (Fig. 3a) as well as in the lung, heart and kidney but not in the brain (Extended Data Fig. 3a). In *sphinx* mice, we found increased p21 in the spleen, liver and lung, but not in the kidney, heart or brain (Fig. 3a,b and Extended Data Fig. 3a). We first examined splenic CD4$^+$ T cells as *sphinx* mice exhibit a near absence of CD8$^+$ T cells in the peripheral lymphoid organs[15]. We found that levels of the senescence markers, p21, p53, p16 and SA-β-gal activity were significantly higher in CD4$^+$ T cells from *sphinx* (7–12-week-old) mice compared to littermate control T cells, in a pattern resembling T cells from aged (16–19-month-old) wild-type (WT) mice (Fig. 3c). We then examined ECs, the principal non-lymphoid subtypes expressing Gimap5, from the liver and lung[9]. We found that CD45$^-$CD31$^+$ liver ECs from *sphinx* mice showed increased p21, p53, p16 and SA-β-gal activity (Fig. 3d). Moreover, p53, p16 and SA-β-gal activity, but not p21 were elevated in liver ECs from aged 16–19-month-old WT mice (Fig. 3d). In CD45$^-$CD31$^+$ lung ECs from *sphinx* mice, the levels of p21 and p53, but not p16 and SA-β-gal activity, were increased (Extended Data Fig. 3b). In contrast, the lung ECs of the aged WT mice did not show increased p21 or p53 but instead had elevated p16 and SA-β-gal activity, suggesting that regulation of senescence pathways is not uniform and may be tissue specific (Extended Data Fig. 3b). Further examination of Gimap5 deficiency in *Rag1*-deficient mice, which lack lymphocytes[9], showed markedly increased p21 in the liver, but not in the spleen (Fig. 3e,f). This indicates that, in contrast to recent reports, the increased senescence in liver ECs in this instance is not induced by adaptive immune cells[32]. Therefore, our findings suggest that Gimap5 deficiency in mice induces senescence in T cells and ECs.

GIMAP5 is essential for CER homeostasis in T cells

Similar to patients who are GIMAP5 deficient, previous work has shown that Gimap5-deficient mice have T cell lymphopenia with abnormally increased T_{EM} cells[14,15]. As the T_{EM} cells predominating in KO mice are not phenotypically comparable to naive T cells in age-matched WT mice,

https://doi.org/10.1038/s41590-023-01691-y

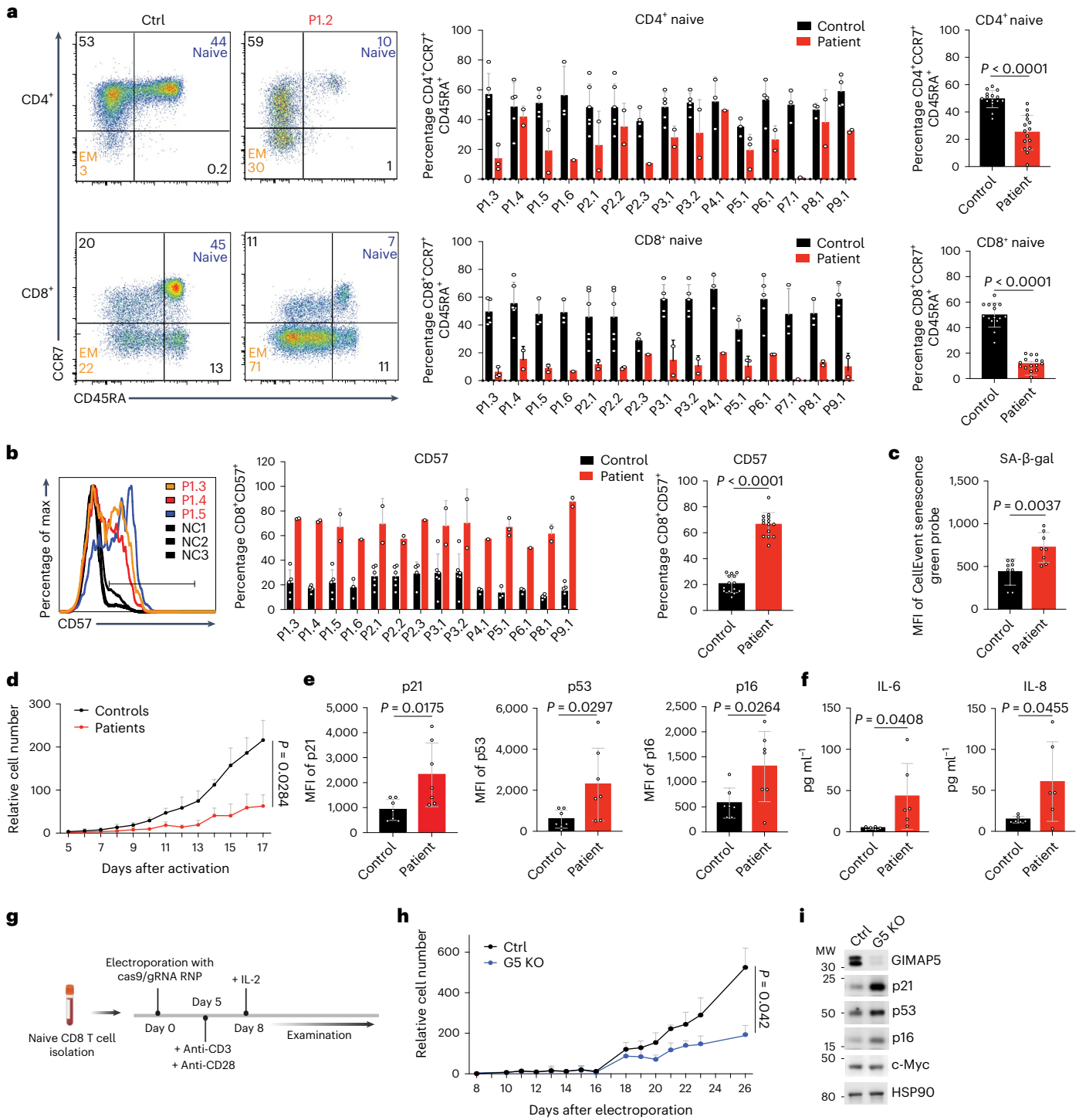


Fig. 2 | GIMAP5 deficiency induces senescence in human lymphocytes. a, Flow cytometry of CD45RA and CCR7 in CD4$^+$ (top) or CD8$^+$ (bottom) T cells from P1.2 and Ctrl (left). Percent of naive CD45RA$^+$CCR7$^+$ in CD4$^+$ or CD8$^+$ T cells from NCs ($n = 53$) and patients ($n = 15$, middle). Means of control and patient data from the middle (right). **b**, Flow cytometry of CD57 on patient CD8$^+$ T cells (P, colors, $n = 51$) compared to NCs (black, $n = 14$) (left). Quantification of gated CD57$^+$CD8$^+$ T cells (middle). Means of control and patient data from the middle (right). **c**, Mean fluorescence intensity (MFI) of SA-β-gal activity in CD8$^+$ T cells from NCs ($n = 16$) and patients ($n = 11$). Points on the control bar represent the mean of matched NCs. **d**, Relative T cell numbers of NCs ($n = 11$) and patients ($n = 8$) after stimulation with anti-CD3/CD28. **e**, MFI of p21, p53 and p16 gated on CD8$^+$ T cells of NCs and patients. p21, NCs ($n = 11$) and patients ($n = 8$); p53, NCs ($n = 16$) and patients ($n = 7$); and p16, NCs ($n = 16$) and patients ($n = 7$). **f**, Serum levels of IL-6 and IL-8 in NCs ($n = 22$) and patients ($n = 6$). **g**, Scheme of naive CD8$^+$ T cells from healthy donor PBMCs electroporated for CRISPR/Cas9 KO of *GIMAP5* (G5 KO). **h**, Relative cell numbers of G5 KO and Ctrl human CD8$^+$ T cells after CD3/CD28 stimulation ($n = 5$ per group). **i**, Representative immunoblot of GIMAP5, p21, p53, p16 and c-Myc with an HSP90-loading control in Ctrl or G5 KO human T cells. Whole-cell lysates were collected on day 16 post-electroporation ($n = 5$). All data are mean ± s.d. and were analyzed by two-tailed, unpaired Student's *t*-test (**a**–**f**,**h**). $P < 0.0001$: $P = 5.81 \times 10^{-6}$, $P = 5.60 \times 10^{-14}$ (**a** top to bottom) and $P = 2.60 \times 10^{-14}$ (**b**).

we investigated acute CRISPR/Cas9 KO of *Gimap5* (Gimap5^{CrKO}) compared to *Thy1.1* KO as a control (Ctrl) in the same cell preparations to assess Gimap5 function using murine T cell blasts (Fig. 4a and Extended Data Fig. 4a). We observed that Gimap5^{CrKO} T cells died over 3 d as the Gimap5 protein was eliminated which recapitulated the T lymphocyte loss in vivo in Gimap5-deficient mice (Fig. 4b)[15,16,21]. Scanning and transmission electron microscopy showed membrane breakdown, indicating necrotic death (Fig. 4c)[33].

Next, we performed metabolomic analysis on Gimap5^{CrKO} T cells due to the pivotal role of metabolism in lymphocyte function and longevity[34]. Mass spectrometry (MS) analysis revealed a surprising increase in CER species across a broad range of lipid subclasses in Gimap5^{CrKO} T cells (Fig. 4d). We verified these results with targeted MS sphingolipid (SPL) analyses that showed specific abnormal increases in very long chain (VLC), 18 and 24 carbon, fatty acid (FA) CER conjugates in Gimap5^{CrKO} T cells (Fig. 4e). We also found elevated dihydroceramides (DCERs), the immediate precursors of CER for de novo synthesis, but reduced hexosylceramides (HCERs), including β-galactosylceramide (GalCER) and β-glucosylceramide (GlcCER) (Fig. 4e). Most of the 16 to 22 carbon FA species of triacylglycerides (TAGs) were also increased (Extended Data Fig. 4b).

TCR stimulation caused death in CD4$^+$ T cells isolated from the *sphinx* mice (Extended Data Fig. 4c)[15,21]. Of note, TCR stimulation of WT cells increased several VLC CERs (C20–C24) (Extended Data Fig. 4d) but there was a sustained overaccumulation of both long-chain (LC) and VLC CERs and a partial reduction of HCERs in *Gimap5*$^{sph/sph}$ CD4$^+$ T cells following TCR stimulation, suggesting that Gimap5 regulates SPL homeostasis in a TCR-dependent manner (Extended Data Fig. 4d). Furthermore, we found that retroviral-mediated expression of the Gimap5^{WT} protein can rescue the survival of activated *Gimap5*$^{sph/sph}$ CD4$^+$ T cells, whereas expression of mutants that either inactivate (Gimap5^{S40N}, unable to bind nucleotides) or constitutively activate (Gimap5^{R121D}, unable to hydrolyze GTP) the enzymatic activity of GTPases[11] could not (Extended Data Fig. 4e–g). Thus, it is evident that proper regulation of the GTP hydrolysis of Gimap5 is required for its function.

Of note, the CERS inhibitor, fumonisin B1 (FB1) reversed CER and DCER accumulation and prevented cell death, indicating that CER accumulation causes Gimap5-deficient T cell demise (Fig. 4f and Extended Data Fig. 4h). Due to the stringent regulation of SPL metabolism, which involves the counter-regulation of CER expression[33], we observed that the KO of *Cers2*, the most abundant Cers in murine T cells (Extended Data Fig. 4i) caused compensatory upregulation of other Cers isoforms, specifically Cers3 and Cers6 (Extended Data Fig. 4j,k). Further in-depth lipidomic analysis of the Cers2 KO murine T cells, revealed a decrease in C22–C26 FA CER/DCERs but an increase in several other CER species, HCERs and sphingomyelin (SM) containing C16–C20 fatty acids, suggesting that this shift in the distribution of CERs and other sphingolipids likely hinders the rescue of Gimap5^{CrKO} T cell death by Cers2 KO (Extended Data Fig. 4l,m). Furthermore, we found that administration of conduritol-β-epoxide (CBE), which induces HCER but not CER accumulation did not rescue Gimap5^{CrKO} T cells indicating that the decreased HCER did not shorten the lifespan of the Gimap5^{CrKO} T cells (Extended Data Fig. 5a,b). Additionally, we observed that zVAD (a pan-caspase inhibitor), necrostatin-1 (a necroptosis inhibitor) and ferrostatin-1 and liproxstatin-1 (ferroptosis inhibitors) were unable to rescue the Gimap5^{CrKO} T cells from cell death (Extended Data Fig. 5c), suggesting that Gimap5^{CrKO} T cells do not undergo apoptosis, necroptosis (necrosis mediated by RIP kinase) or ferroptosis as their mode of cell death.

CER has been implicated in the induction of cellular senescence and aging[35]. Hence, we hypothesized that chronically high levels of CER in Gimap5-deficient cells cause senescence in CD4$^+$ T cells from *sphinx* mice (Fig. 3c). Given the CER abnormalities in *sphinx* mice, we next examined the lipidomic profiles in GIMAP5-deficient patient T cells. The requirements for multiple additional samples were challenging for the study participants, but of the nine families contacted, we successfully obtained sufficient samples from three families. We detected elevated species of VLC CERs in GIMAP5-deficient patient T cells, for example P2.2 and P7.1, which were very similar to what we observed in mice (Fig. 4g). Several VLC SPL, including SM species, were also elevated in patients but not in family members or controls (Fig. 4g and Extended Data Fig. 5d)[35]. Notably, we detected decreased CER/DCER but elevated HCER in GIMAP5-deficient T cells from P1.4 who currently has no symptoms (Extended Data Fig. 5d). Thus, mice and humans exhibited comparable abnormal CER accumulation when GIMAP5 was deficient. We next examined whether increased senescence markers in human GIMAP5^{CrKO} T cells (Fig. 2i) were CER-dependent. Our findings show that CERS suppression by FB1 significantly reduces p21 and p53 levels in GIMAP5^{CrKO} T cells, implying that GIMAP5 induces T cell senescence by modulating CER (Extended Data Fig. 5e); however, we did not observe an increase in p21 in the Gimap5^{CrKO} murine T cells, which are undergoing cell death starting on day 2 after electroporation (Fig. 4b and Extended Data Fig. 5f). This suggests that the lack of senescent cells may be due to these cells proceeding directly to cell death. A comparison of GIMAP5 deficiency in mouse and human T cells revealed a difference: human T cells survived better than mouse cells but became senescent and non-proliferative (compare Extended Data Fig. 2o to Fig. 4b); however, the defect in cell and organismal longevity is likely attributable to cellular senescence in both humans and mice. Hence, GIMAP5 deficiency disrupts CER homeostasis in T cells, leading to cell death or senescence.

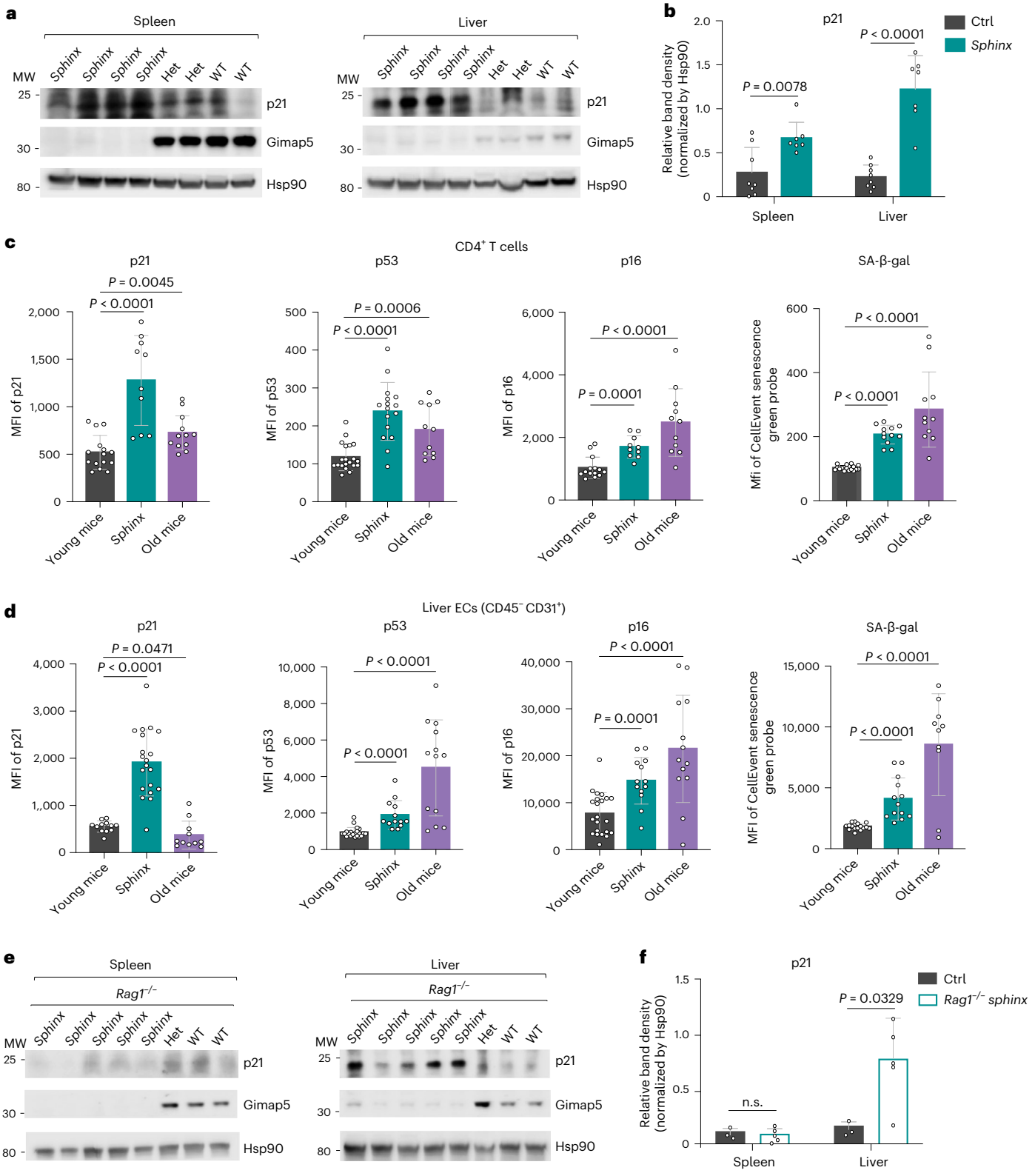
GIMAP5 controls CER levels through CK2

To understand the molecular mechanism by which GIMAP5 controls CER accumulation, we examined GIMAP5 interactors using GST pull-down and MS. We detected a GIMAP5 signal, indicating that GIMAP5 homodimerizes as expected for dynamin/septin-like GTPases[10,11,18] (Fig. 5a). We also found the principal interactor to be LCK, explaining how TCR signals induce the diseased T cell phenotype in GIMAP5 deficiency[21], and two isoforms of the catalytic subunits of protein kinase CK2 (CK2) (CK2α/CSNK2A1 and CK2α′/CSNK2A2) (Fig. 5a). CK2 is a constitutively active serine/threonine kinase that regulates cell differentiation, proliferation and survival[36,37]. The holoenzyme CK2

Fig. 3 | Gimap5 deficiency in mice induces senescence in T cells and liver endothelial cells. a, Spleen (left) and liver (right) tissue lysates from *Gimap5*$^{sph/sph}$, *Gimap5*$^{+/sph}$ (Het) and WT mice were immunoblotted for indicated proteins ($n = 2$). **b**, Quantification of p21 bands in **a** using ImageJ. Controls ($n = 8$), *sphinx* ($n = 7$). **c**, MFI of p21, p53, p16 and SA-β-gal activity gated on CD4$^+$ T cells from *sphinx*, young and aged WT mice. CD4$^+$p21, young ($n = 15$), *sphinx* ($n = 10$), aged ($n = 11$) mice; CD4$^+$p53, young ($n = 20$), *sphinx* ($n = 16$), aged ($n = 11$) mice; CD4$^+$p16, young ($n = 14$), *sphinx* ($n = 10$), aged ($n = 11$) mice; CD4$^+$SA-β-gal, young (n = 17), *sphinx* ($n = 12$), aged ($n = 11$) mice. **d**, MFI of p21, p53, p16 and SA-β-gal activity in CD45$^-$CD31$^+$ liver ECs from young, *sphinx* and aged mice. CD31$^+$p21, young ($n = 13$), *sphinx* ($n = 20$), aged ($n = 11$) mice; CD31$^+$p53, young ($n = 21$), *sphinx* ($n = 13$), aged ($n = 13$) mice; CD31$^+$p16: young ($n = 22$), *sphinx* ($n = 13$), aged ($n = 13$) mice; CD31$^+$SA-β-gal, young ($n = 16$), *sphinx* ($n = 13$), aged ($n = 10$) mice. **e**, Spleen (left) and liver (right) tissue lysates from *Gimap5*$^{sph/sph}$ *Rag1*$^{-/-}$, *Gimap5*$^{+/sph}$ *Rag1*$^{-/-}$ and *Gimap5*$^{+/+}$ *Rag1*$^{-/-}$ mice were immunoblotted for indicated proteins. Controls ($n = 3$), *Gimap5*$^{sph/sph}$ *Rag1*$^{-/-}$ ($n = 5$). **f**, Quantification of p21 bands in **e** using ImageJ. 7–12-week-old (young, *sphinx*) or 16–19-month-old (aged) male and female mice were used in each experiment. Young mice were littermate controls for *sphinx*. All data are mean ± s.d. and were analyzed by two-tailed, unpaired Student's *t*-test (**b**–**d**,**f**). NS, not significant. $P < 0.0001$: $P = 1.03 \times 10^{-5}$ (**b**), $P = 8.67 \times 10^{-6}$, $P = 3.94 \times 10^{-7}$, $P = 8.72 \times 10^{-5}$, $P = 6.10 \times 10^{-14}$ (**c** left to right) and $P = 1.31 \times 10^{-7}$, $P = 1.34 \times 10^{-5}$, $P = 6.64 \times 10^{-7}$, $P = 1.44 \times 10^{-5}$, $P = 1.71 \times 10^{-5}$, $P = 1.04 \times 10^{-6}$ (**d** left to right).

https://doi.org/10.1038/s41590-023-01691-y

consists of two catalytic subunits (α and/or α′) and two copies of the regulatory subunit (β), forming either $\alpha_2\beta_2$, $\alpha'_2\beta_2$ or $\alpha\alpha'\beta_2$ tetramers[36,37]. STRING analysis showed that multiple GIMAP5 interactors (mean $\log_2$ ratio >2) were either CK2 substrates or interactors (Fig. 5a)[38]. Notably, CK2 has been described to phosphorylate and activate CERS in the endoplasmic reticulum (ER)[39], suggesting a potential link between GIMAP5 and the regulation of CER synthesis. Therefore, we examined whether GIMAP5 controls CK2. Immunoprecipitation (IP) of epitope-tagged proteins showed that GIMAP5 interacted with CK2α and CK2α′, but not CK2β (Extended Data Fig. 6a). We further assessed the interaction of CK2α with GIMAP5 full-length (FL) or truncation mutants lacking the G domain (GIMAP5 NΔ) or C-terminal hydrophobic domain (GIMAP5 CΔ) by overexpressing FLAG-tagged proteins in 293T cells (Extended Data Fig. 6b). We found that GIMAP5 FL or NΔ interacts strongly with CK2α, whereas GIMAP5 CΔ has almost no interaction, suggesting that GIMAP5 requires both its hydrophobic domain for



https://doi.org/10.1038/s41590-023-01691-y

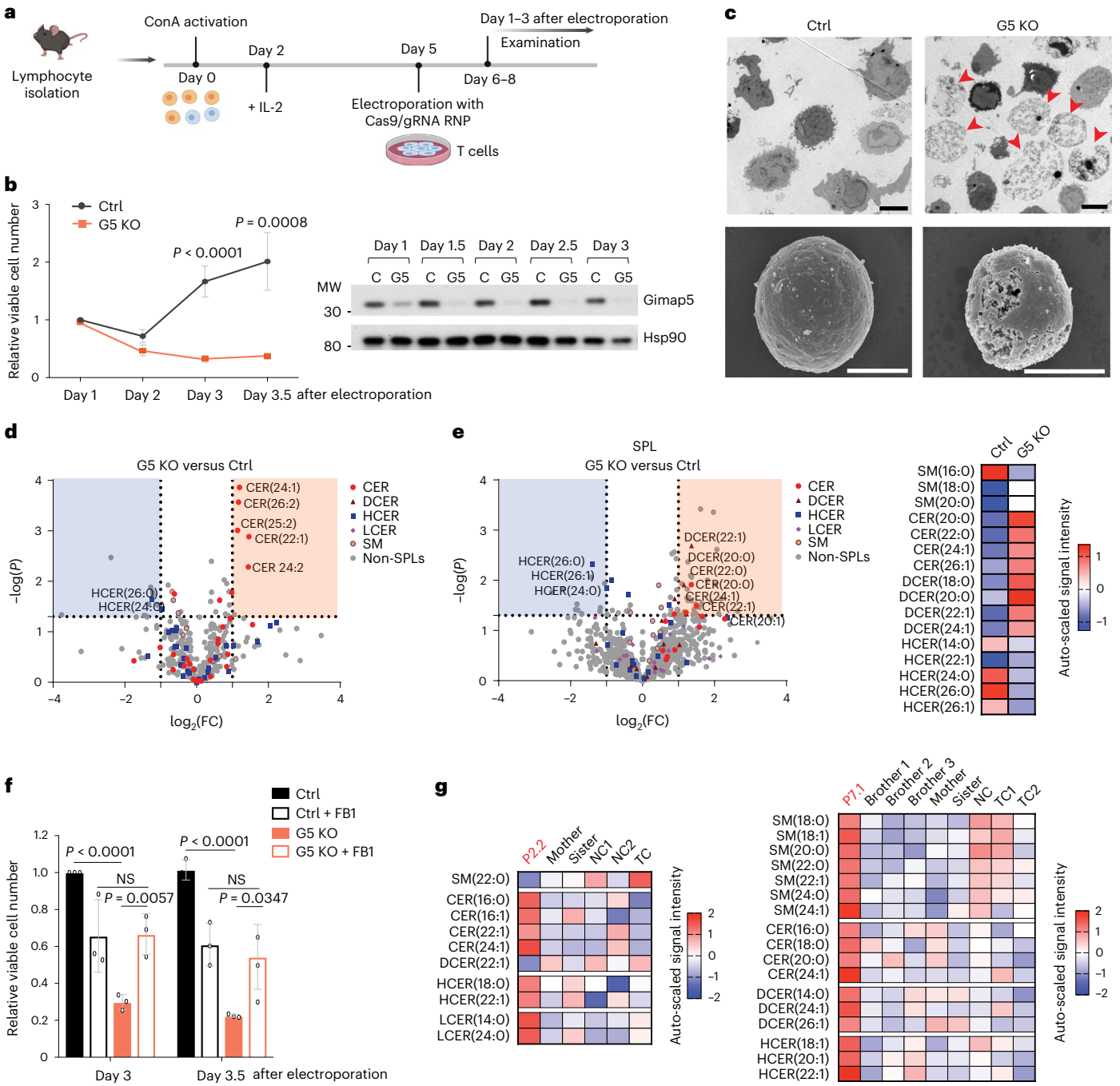


Fig. 4 | GIMAP5 is essential for CER homeostasis in T cells. a, Schematic for isolating lymphocytes from 8–12-week-old C57BL/6 mouse spleens, followed by electroporation on day 5 after starting concanavalin A (ConA) and IL-2 stimulation for CRISPR/Cas9 KO of Gimap5 (G5 KO) or control (Ctrl). gRNA, guide RNA; RNP, ribonucleoprotein. **b**, Relative viable number from **a** over time (left). Note that electroporation induces modest Ctrl cell death for 1–2 d. Lysates were immunoblotted for indicated proteins (right) ($n = 5$). C, Ctrl; G5, G5 KO. **c**, Transmission (top) and scanning (bottom) electron microscopic images of cells from **a** on day 3 post-electroporation ($n = 3$). Scale bars, 5 µm. Red arrows indicate necrotic cell corpses. **d**,**e**, Volcano plots of lipids detected by untargeted (**d**) or targeted (**e**) (left) MS analysis of G5 KO versus Ctrl. Families of SPLs are indicated by shape and color. Dotted lines indicate a P value of 0.05 and $\log_2$ fold change (FC) of 1 or −1 (**d** and **e**, left). Significantly reduced SPLs are shown in blue fields and increased SPLs are shown in orange fields. Heat map of signal intensity of SPLs (**e**, right). Displayed are SPLs that pass a P value cutoff of 0.05 by t-test. Signals reflect the total sum normalized, auto-scaled signal intensity ($n = 5$). Lipid designation is shown (chain length: no. of unsaturated bonds). LCER, lactosylceramide. **f**, Relative viable cell number of Ctrl and G5 KO murine T cells treated with fumonisin B1 (FB1) (5 µM, 48 h) on day 1 and quantified on day 3 or 3.5 post-electroporation ($n = 3$ per group). **g**, Heat map of SPLs detected in P2.2 (left) and P7.1 (right), healthy family members, NCs or shipping controls (TCs). All hits on the heat maps are features that are >1 s.d. from the mean (>1 z score) ($n = 3$). All data are mean ± s.d. and were analyzed by two-tailed, unpaired Student's t-test (**b**,**d**–**f**). NS, not significant. $P < 0.0001$: $P = 6.42 \times 10^{-5}$ (**b**) and $P = 8.15 \times 10^{-6}$, $P = 1.59 \times 10^{-5}$ (**f** left to right).

proper localization to engage with CK2α and its coiled-coil domain for interaction with CK2α (Extended Data Fig. 6c). Correspondingly, native endogenous CK2α co-immunoprecipitated with GIMAP5, LCK and CK2β kinetically after TCR activation (Fig. 5b). CK2α is constitutively associated with CK2β but GIMAP5 and LCK are most abundantly recruited to the complex at 15–30 min of TCR stimulation (Fig. 5b). Furthermore, as the peak TCR-induced association of CK2α with GIMAP5 and LCK diminishes, the CK2 complex switches at 90 min to recruitment of the enzyme CERS2 that synthesizes VLC CER (Fig. 5b). Thus, TCR-induced generation of CER may result from CK2-mediated CERS2 activation. Notably, the level of p21, a senescence mediator, increased at 90 min after TCR stimulation, the same time as the increased CK2α–CERS2 interaction (Fig. 5b) and FB1 treatment inhibited the late TCR-induced elevation of p21 (Extended Data Fig. 6d)[35]. Using proximity ligation analysis, we verified that GIMAP5 transiently associates with CK2α in intact cells in a time course consistent with the complex observed by co-IP (Extended Data Fig. 6e and Fig. 5b). Additionally, we confirmed that endogenous GIMAP5 co-immunoprecipitated CK2α, LCK and CERS2 in response to TCR activation (Extended Data Fig. 6f).

Next, we examined the subcellular localization of GIMAP5, LCK and CK2α complex. We found that GIMAP5 colocalizes with late endosome/lysosomal markers, LAMP1, Rab7 and LAMTOR4 and partially colocalizes with the endoplasmic reticulum (ER) marker, calnexin, whereas no colocalization was detected with MitoTracker in human T cell blasts (Extended Data Fig. 7a). Furthermore, we observed that LCK adopts a notable punctate pattern upon TCR stimulation implying it is associated with vesicles (Fig. 5c and Extended Data Fig. 7b). Some LCK vesicles colocalize with GIMAP5 and Rab7 following TCR stimulation, whereas GIMAP5 exhibited constitutive colocalization with Rab7 (Extended Data Fig. 7b). These findings suggest that LCK traffics to late endosomes and partially colocalizes with GIMAP5 after TCR stimulation. The colocalization of CK2α with GIMAP5 and LCK also increased after TCR stimulation (Fig. 5c and Extended Data Fig. 7c), which aligned with our co-IP data (Fig. 5b). As reported in previous studies, CK2 has been suggested to phosphorylate the C-terminal segment of CERS at the cytosolic face of the ER membrane[39]. Thus, it is conceivable that GIMAP5 and CK2 interact at the contact site between the ER and late endosome/lysosome. We observed the colocalization of CK2α with both calnexin and Rab7 (Extended Data Fig. 7c,d), and following TCR stimulation, CK2α exhibited reduced colocalization with calnexin while maintaining stable colocalization with Rab7 (Extended Data Fig. 7c,d). Of note, partial CK2α colocalization with another late endosomal marker, LAMTOR4, was increased (Fig. 5d and Extended Data Fig. 7c,e). These findings indicate that CK2α binds to GIMAP5 after TCR stimulation at the late endosome, possibly near sites of association with the ER. This provides a plausible mechanism by which TCR signaling regulates CER levels at the contact site between the ER and late endosome/lysosome.

Notably, lipidomic analyses showed a transient elevation of CERs in response to TCR stimulation in control T cells, whereas GIMAP-5^{CrKO} human T cells showed the persistent increase in most CERs until 240 min after TCR stimulation (Fig. 5e), similar to what we observed in *Gimap5*$^{sph/sph}$ murine T cells (Extended Data Fig. 4d), highlighting the TCR-dependent regulation of CER by GIMAP5. We therefore hypothesized that GIMAP5 negatively controls the association of CERS2 with CK2. Indeed, whereas the Ck2α–Cers2 interaction required TCR stimulation in Thy1.1^{CrKO} control T cells, this interaction was constitutive and sustained at a high level in Gimap5^{CrKO} T cells (Fig. 5f). In contrast, the interaction of Ck2α with Ck2β and LCK, pErk induction and the level of CK2α were not affected (Fig. 5f and Extended Data Fig. 8a–d).

Consistent with our hypothesis, the double CRISPR/Cas9 KO of *Csnk2a1* (*CK2a1*) and *Gimap5* partially rescued cell viability although Csnk2a1^{CrKO} T cells showed reduced viability compared to Thy1.1^{CrKO} T cells as previously reported (Fig. 5g)[36]. Also, TCR-induced death of Gimap5^{CrKO} T cells was attenuated by the CK2 chemical inhibitor, CX-4945 (Fig. 5h). Moreover, CX-4945 treatment strongly inhibited the accumulation of VLC CERs in Gimap5^{CrKO} T cells (Fig. 5i), validating the hypothesis that CK2 plays a role in the uncontrolled CER accumulation that leads to Gimap5^{CrKO} T cell death. Additionally, we found that several lipid abnormalities involving DCER, HCER and TAGs were reversed after CX-4945 treatment of Gimap5^{CrKO} T cells, indicating that GIMAP5/CK2 is a key lipid regulatory axis for T cells (Fig. 5i and Extended Data Fig. 8e). We also found that CX-4945 potently suppresses levels of p21 and p53 in both control and GIMAP5^{CrKO} T cells, showing that the GIMAP5–CK2 axis governs human T cell senescence (Fig. 5j and Extended Data Fig. 8f)[35]. Of note, TCR-induced elevation of CERs and p21 in human primary T cell blasts was potently reversed by CX-4945 treatment (Fig. 5k and Extended Data Fig. 8g). Hence, GIMAP5 regulates a TCR-induced LASS metabolic pathway through CK2 that plays a critical role in the regulation of T cell longevity and senescence.

Finally, to directly illustrate the effects of the GIMAP5 pathway on CER, we administered C6-CER to WT human T cell blasts. C6-CER was previously shown to induce cell death or senescence in a time- and concentration-dependent manner by stimulating CERS to generate LC CERs[40,41]. Increased endogenous CERs are caused by the deacylation of C6-CER to sphingosine, which is enzymatically reacylated by CERS in an FB1-inhibitable reaction to generate toxic overaccumulation of CER (Fig. 6a)[40]. We observed that C6-CER induces cell death in T cells but does not significantly induce senescence (Fig. 6b–d to Extended Data Fig. 9a–f). We found that both FB1 and CX-4945 reduced the lethal effects of C6-CER administration (Fig. 6b,c). Of note, we overexpressed GIMAP5 protein using a lentiviral vector in T cells and found that it similarly reduced C6-CER lethality (Fig. 6d). These data confirmed the central role of GIMAP5 in CER homeostasis. Thus, our findings demonstrate that GIMAP5 is essential for maintaining CER homeostasis by restricting CK2 activation of CERS, which in turn affects cellular senescence and lifespan (Fig. 6e and Extended Data Fig. 10).

Discussion

As aging-related diseases continue to increase worldwide, it is crucial to investigate longevity pathways in humans that may enhance healthspan. SPLs, especially CERs, have been implicated in the regulation of cell senescence, proliferation, differentiation and survival in multiple cell types and organisms[4]. CERs have also been implicated in aging and the pathogenesis of age-related diseases, including type 2 diabetes, cancer, cardiovascular diseases and neurodegeneration[35]. Our finding represents new evidence of the link between CER and T cell immunosenescence and establishes a new regulatory axis involving CK2, CERS2 and GIMAP5.

GIMAP5 is the best-known member of the GIMAP gene family, but its deficiency causes severe immune pathology that is poorly understood. For example, it is the gene underlying lymphopenia and autoimmunity associated with characteristic congenital diabetes in the BB rat, the targeted gene in *sphinx* severely lymphopenic mice and a putative deleterious variant previously observed in a single immunodeficient individual[8,13–16,21]. Therefore, it is important to understand how GIMAP5 ensures the vitality of T lymphocytes in mice, rats and humans and its cellular function as a GTPase tethered to internal vesicles, lysosomes and ER membranes[42]. Early reports of GIMAP5 regulating Bcl-2, lysosomal Ca^{2+} and mTOR activity have been contested[18–20]. Many of these earlier studies used isolated cells from animals with systemic immune dysregulation, whereas our CRISPR-mediated acute *GIMAP5* KO model enabled us to identify the specific biochemical functions of GIMAP5 using the same populations of cells as the control.

We find that GIMAP5 deficiency causes a new human genetic immunodeficiency disease with a lymphopenia phenotype and reveal its critical biochemical role in lipid homeostasis to ensure cell longevity and prevent senescence. We now call this disease 'GIMAP5 deficiency with immunodysregulation, splenomegaly, enlarged lymph nodes, liver disease and lymphopenia' (GISELL; pronounced with a soft

https://doi.org/10.1038/s41590-023-01691-y

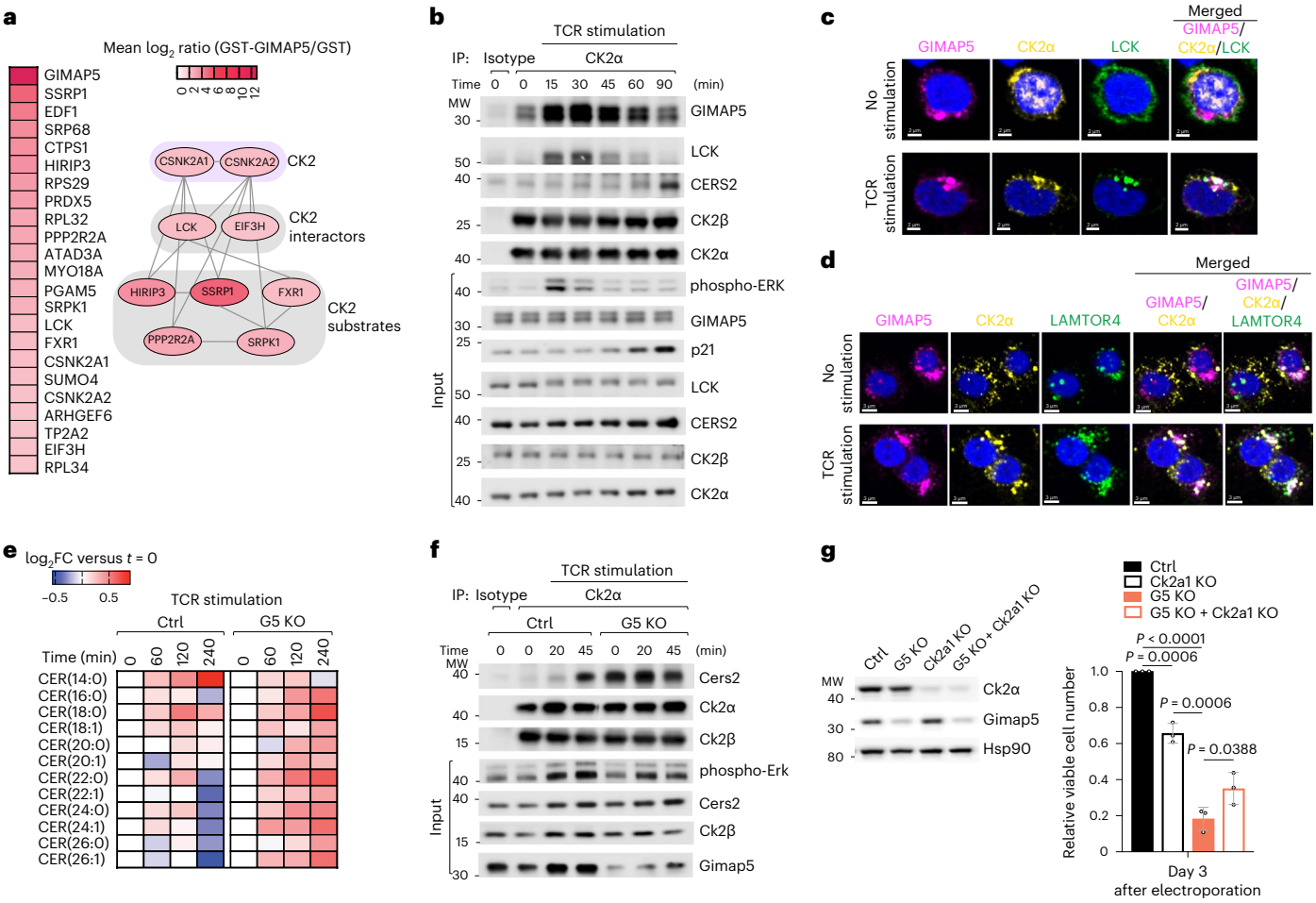


Fig. 5 | GIMAP5 associates with CK2 and regulates CER levels. a, MS analysis of GST-GIMAP5-binding proteins represented as a heat map (left). GIMAP5 interactors that have been found as either CK2 substrates or interactors are labeled in bold (left) and visualized using CytoScape software (right). Proteins with a mean $\log_2$ ratio > 2 are displayed after CRAPome filtration[49]. Color intensity reflects the mean $\log_2$ ratio (top scale). **b**, Immunoblots of IP with anti-CK2α or isotype control and the input in human T cell blasts after TCR stimulation shown in minutes (min) ($n = 4$). **c**,**d**, Immunofluorescence staining with anti-GIMAP5 (magenta), CK2α (yellow) and LCK (green in **c**) or LAMTOR4 (green in **d**) in human T cell blasts before and after TCR stimulation (60 min) ($n = 3$). **e**, Heat map of the $\log_2$ FC of CERs in human T cell blasts after TCR stimulation ($n = 7$). Each group is normalized to time 0. **f**, Immunoblots of the IP of Ck2α (top) and the input lysate (bottom) in Ctrl or G5 KO murine T cell blasts on day 3 post-electroporation after stimulation ($n = 4$). **g**, Immunoblots of Ctrl KO, G5 KO, G5 KO + Ck2a1 KO murine T cell lysates for proteins shown on day 3 post-electroporation (left). Relative viable cell numbers from left (right) ($n = 3$ per group). **h**, Relative viable cell numbers on day 3 and 3.5 post-electroporation of Ctrl and G5 KO murine T cells treated with CX-4945 (2.5 μM), started on day 1 ($n = 3$ per group). **i**, Heat map of SPLs from **h**. SPLs significantly affected in Fig. 4e are displayed ($P \leq 0.05$) ($n = 3$). Yellow box indicates key downregulated species. **j**, Immunoblots of cell lysates treated with CX-4945 (2.5 μM, 24 h) for proteins shown ($n = 4$). **k**, Heat map of CERs in human T cell blasts without or with CX-4945 (2.5 μM) followed by TCR stimulation ($n = 3$). Each sample is normalized to time 0. DMSO, dimethylsulfoxide. All data are mean ± s.d. and were analyzed by two-tailed, unpaired Student's *t*-test (**g**,**h**). $P < 0.0001$: $P = 2.51 \times 10^{-5}$ (**g**).

https://doi.org/10.1038/s41590-023-01691-y

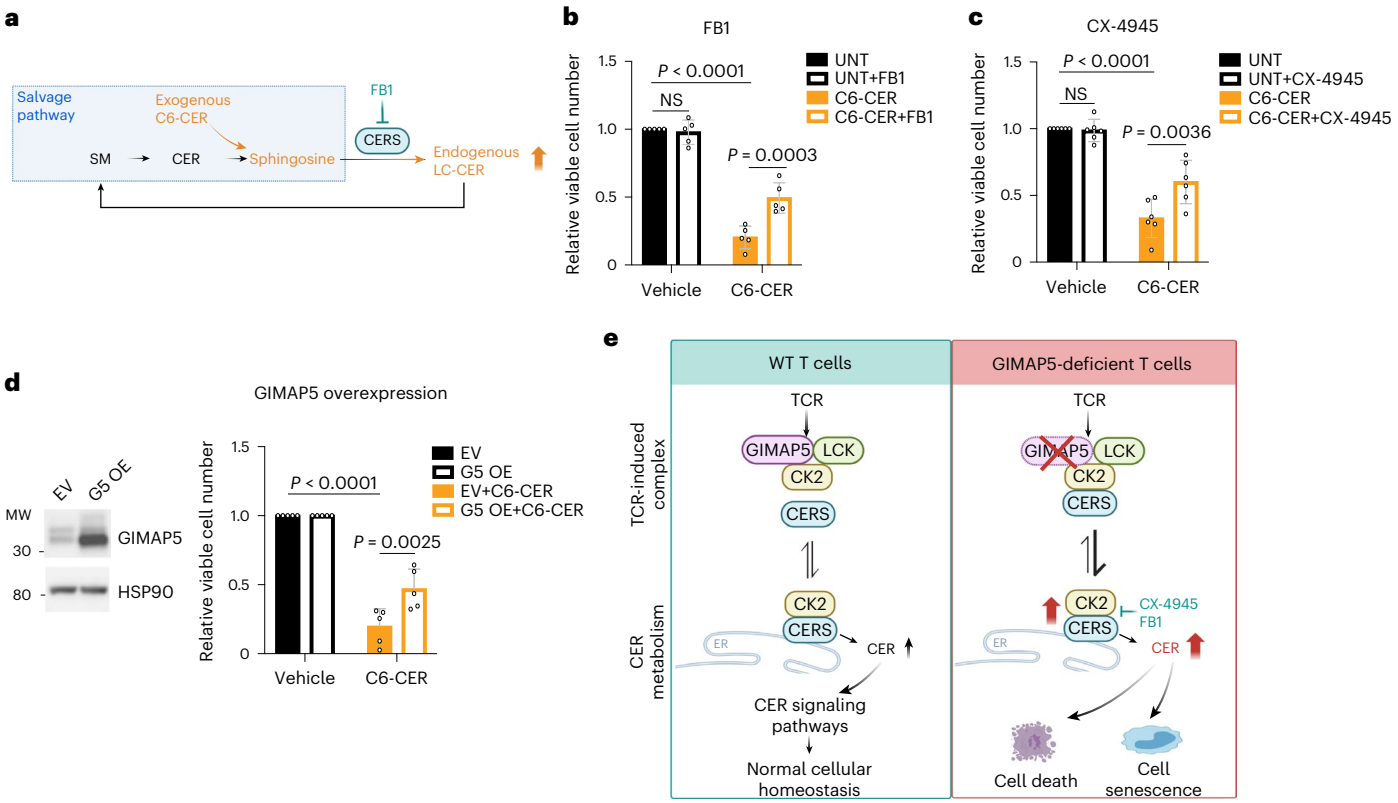


Fig. 6 | CK2 inhibition and GIMAP5 overexpression in T cells rescue the cell death induced by the accumulation of endogenous CERs. a, Diagram of the generation of endogenous LC CERs by treating cells with exogenous C6-CER. **b**,**c**, Relative viable cell numbers of untreated (UNT) and C6-CER-treated (Avanti Polar lipid, 35 μM, 24 h) human T cell blasts with and without FB1(**b**) and CX-4945 (**c**). FB1, 10 μM ($n = 5$ per group); CX-4945, 2.5 μM ($n = 5$ per group). **d**, Immunoblot of GIMAP5 with an HSP90-loading control in lentivirus-mediated either empty vector (EV) or GIMAP5 overexpression (G5 OE) in human T cells (left, $n = 5$ per group). Relative viable cell numbers of EV or GIMAP5 (G5) lentivirus-transduced human T cell blasts with or without C6-CERs treatment (32.5 μM, 24 h) (right, $n = 5$ per group). **e**, A model of GIMAP5 regulating TCR-induced CER levels through CK2, thereby affecting T cell longevity and senescence. All data are mean ± s.d. and were analyzed by two-way analysis of variance (ANOVA) with Bonferroni post-test correction (**b**–**d**). $P < 0.0001$: $P = 4.11 \times 10^{-10}$ (**b**), $P = 1.83 \times 10^{-8}$ (**c**) and $P = 3.47 \times 10^{-9}$ (**d**).

G; (/dʒɪˈzɛl/). We find that GIMAP5 governs CER levels by controlling CK2–CERS2 association in lymphocytes. The absence of GIMAP5 allows for their constitutive interaction causing CER accumulation and consequential cell senescence or death. Thus, our discovery demonstrates that the dysregulation of CER homeostasis is the underlying cause of the immunodeficiency resulting from the loss of GIMAP5 function, which is primarily attributed to its vital and distinct role in regulating T cell longevity. Murine T cells lacking Gimap5 progress rapidly through senescence to overt death. Therefore, it has been especially important to study GIMAP5 deficiency in humans as it is slower to induce death and yields T cells in a senescence phenotype that might be reversible with appropriate pharmaceuticals. It was not possible to study the pathway in immortalized cell lines such as Jurkat or HuT 78 because GIMAP5 deletion had no discernible effect, likely because immortalization circumvents cellular senescence and death processes. The defects caused by GIMAP5 deficiency are rescued by CK2 inhibition thus CX-4945 or other similar drugs may be effective as treatment options for GISELL, which has a very high mortality[43,44].

A recent report showed that GIMAP5 deficiency in both humans and mice causes capillarization of liver sinusoidal endothelial cells (LSECs), which contributes to liver portal hypertension[9]. Although the mechanism of LSEC capillarization is currently unknown, vascular endothelial growth factor (VEGF)-mediated nitric oxide (NO) signaling has been implicated in the maintenance of LSEC fenestrae[45]. As CER has been shown to promote vasoconstriction by regulating NO signaling, future research on the roles of CER and GIMAP5 in NO signaling of LSECs could provide new insight into the underlying mechanism of portal hypertension[46].

Finally, there are broader implications for understanding this pathway in different tissues as overall cell vitality and function diminish greatly with aging and senescence[47]. The presumed consequences of immune senescence were evident globally in many different populations during the current COVID-19 pandemic, which showed a strong age-related mortality[48]. Cellular senescence likely underlies the general vulnerability of the elderly to various diseases, and this will be an increasing health burden as the aging population increases globally. Our data show that similar senescence changes occur in ECs and T cells from aged mice as those we found in GIMAP5-deficient cells. We now show how to modulate the LASS pathway, which could be useful to enhance protective immunity, vaccination efficiency or immunotherapy, and potentially deploy the pathway in cases of autoimmunity or allograft rejection. The riddle of the sphinx was a metaphor for the changes caused by aging during human life. The *sphinx* mouse now reveals how the processes of aging can be regulated by lipid homeostasis, especially in lymphocytes. Our discovery of a regulatory axis linking CK2, CERS2 and GIMAP5 provides new biochemical insights on how to keep mammalian T cells alive and youthful.

Online content

Any methods, additional references, Nature Portfolio reporting summaries, source data, extended data, supplementary information, acknowledgements, peer review information; details of author contributions

and competing interests; and statements of data and code availability are available at https://doi.org/10.1038/s41590-023-01691-y.

References

1. Ohtsuka, H., Shimasaki, T. & Aiba, H. Genes affecting the extension of chronological lifespan in *Schizosaccharomyces pombe* (fission yeast). *Mol. Microbiol.* **115**, 623–642 (2021).
2. Jiang, J. C., Kirchman, P. A., Allen, M. & Jazwinski, S. M. Suppressor analysis points to the subtle role of the LAG1 ceramide synthase gene in determining yeast longevity. *Exp. Gerontol.* **39**, 999–1009 (2004).
3. Jiang, J. C., Kirchman, P. A., Zagulski, M., Hunt, J. & Jazwinski, S. M. Homologs of the yeast longevity gene LAG1 in *Caenorhabditis elegans* and human. *Genome Res.* **8**, 1259–1272 (1998).
4. Hannun, Y. A. & Obeid, L. M. Principles of bioactive lipid signalling: lessons from sphingolipids. *Nat. Rev. Mol. Cell Biol.* **9**, 139–150 (2008).
5. Bikman, B. T. & Summers, S. A. Ceramides as modulators of cellular and whole-body metabolism. *J. Clin. Invest.* **121**, 4222–4230 (2011).
6. Kurz, J., Parnham, M. J., Geisslinger, G. & Schiffmann, S. Ceramides as novel disease biomarkers. *Trends Mol. Med.* **25**, 20–32 (2019).
7. Tonnetti, L., Veri, M. C., Bonvini, E. & D'Adamio, L. A role for neutral sphingomyelinase-mediated ceramide production in T cell receptor-induced apoptosis and mitogen-activated protein kinase-mediated signal transduction. *J. Exp. Med.* **189**, 1581–1589 (1999).
8. MacMurray, A. J. et al. Lymphopenia in the BB rat model of type 1 diabetes is due to a mutation in a novel immune-associated nucleotide (Ian)-related gene. *Genome Res.* **12**, 1029–1039 (2002).
9. Drzewiecki, K. et al. GIMAP5 maintains liver endothelial cell homeostasis and prevents portal hypertension. *J. Exp. Med.* **218**, e20201745 (2021).
10. Gasper, R., Meyer, S., Gotthardt, K., Sirajuddin, M. & Wittinghofer, A. It takes two to tango: regulation of G proteins by dimerization. *Nat. Rev. Mol. Cell Biol.* **10**, 423–429 (2009).
11. Schwefel, D. et al. Structural insights into the mechanism of GTPase activation in the GIMAP family. *Structure* **21**, 550–559 (2013).
12. Wong, V. W. et al. The autoimmunity-related GIMAP5 GTPase is a lysosome-associated protein. *Self Nonself* **1**, 259–268 (2010).
13. Cousins, L. et al. Eosinophilic bowel disease controlled by the BB rat-derived lymphopenia/Gimap5 gene. *Gastroenterology* **131**, 1475–1485 (2006).
14. Schulteis, R. D. et al. Impaired survival of peripheral T cells, disrupted NK/NKT cell development, and liver failure in mice lacking Gimap5. *Blood* **112**, 4905–4914 (2008).
15. Barnes, M. J. et al. Loss of T cell and B cell quiescence precedes the onset of microbial flora-dependent wasting disease and intestinal inflammation in Gimap5-deficient mice. *J. Immunol.* **184**, 3743–3754 (2010).
16. Yano, K. et al. Gimap3 and Gimap5 cooperate to maintain T-cell numbers in the mouse. *Eur. J. Immunol.* **44**, 561–572 (2014).
17. Kupfer, R. et al. Loss of a gimap/ian gene leads to activation of NF-κB through a MAPK-dependent pathway. *Mol. Immunol.* **44**, 479–487 (2007).
18. Nitta, T. et al. IAN family critically regulates survival and development of T lymphocytes. *PLoS Biol.* **4**, e103 (2006).
19. Chen, X. L. et al. GIMAP5 deficiency is associated with increased AKT activity in T lymphocytes. *PLoS ONE* **10**, e0139019 (2015).
20. Serrano, D. et al. GTPase of the immune-associated nucleotide protein 5 regulates the lysosomal calcium compartment in T lymphocytes. *Front. Immunol.* **8**, 94 (2017).
21. Patterson, A. R. et al. Gimap5-dependent inactivation of GSK3β is required for CD4(+) T cell homeostasis and prevention of immune pathology. *Nat. Commun.* **9**, 430 (2018).
22. Heinonen, M. T. et al. GIMAP GTPase family genes: potential modifiers in autoimmune diabetes, asthma, and allergy. *J. Immunol.* **194**, 5885–5894 (2015).
23. Hellquist, A. et al. The human GIMAP5 gene has a common polyadenylation polymorphism increasing risk to systemic lupus erythematosus. *J. Med. Genet.* **44**, 314–321 (2007).
24. Lee, Y. J. et al. Genome-wide association study identifies GIMAP as a novel susceptibility locus for Behcet's disease. *Ann. Rheum. Dis.* **72**, 1510–1516 (2013).
25. Schwefel, D. et al. Structural basis of oligomerization in septin-like GTPase of immunity-associated protein 2 (GIMAP2). *Proc. Natl Acad. Sci. USA* **107**, 20299–20304 (2010).
26. Uhlen, M. et al. Proteomics. Tissue-based map of the human proteome. *Science* **347**, 1260419 (2015).
27. Leipold, M. D. & Maecker, H. T. Phenotyping of live human PBMC using CyTOF mass cytometry. *Bio Protoc.* **5**, 1382 (2015).
28. Shearer, W. T. et al. Lymphocyte subsets in healthy children from birth through 18 years of age: the Pediatric AIDS Clinical Trials Group P1009 study. *J. Allergy Clin. Immunol.* **112**, 973–980 (2003).
29. Pawelec, G. Is there a positive side to T cell exhaustion? *Front. Immunol.* **10**, 111 (2019).
30. Seki, A. & Rutz, S. Optimized RNP transfection for highly efficient CRISPR/Cas9-mediated gene knockout in primary T cells. *J. Exp. Med.* **215**, 985–997 (2018).
31. Gire, V. & Dulic, V. Senescence from G2 arrest, revisited. *Cell Cycle* **14**, 297–304 (2015).
32. Yousefzadeh, M. J. et al. An aged immune system drives senescence and ageing of solid organs. *Nature* **594**, 100–105 (2021).
33. Mullen, T. D. & Obeid, L. M. Ceramide and apoptosis: exploring the enigmatic connections between sphingolipid metabolism and programmed cell death. *Anticancer Agents Med. Chem.* **12**, 340–363 (2012).
34. Pearce, E. L., Poffenberger, M. C., Chang, C. H. & Jones, R. G. Fueling immunity: insights into metabolism and lymphocyte function. *Science* **342**, 1242454 (2013).
35. Trayssac, M., Hannun, Y. A. & Obeid, L. M. Role of sphingolipids in senescence: implication in aging and age-related diseases. *J. Clin. Invest.* **128**, 2702–2712 (2018).
36. Ahmed, K., Gerber, D. A. & Cochet, C. Joining the cell survival squad: an emerging role for protein kinase CK2. *Trends Cell Biol.* **12**, 226–CK230 (2002).
37. Pinna, L. A. & Meggio, F. Protein kinase CK2 ('casein kinase-2') and its implication in cell division and proliferation. *Prog. Cell Cycle Res.* **3**, 77–97 (1997).
38. von Mering, C. et al. STRING: known and predicted protein–protein associations, integrated and transferred across organisms. *Nucleic Acids Res.* **33**, D433–D437 (2005).
39. Sassa, T., Hirayama, T. & Kihara, A. Enzyme activities of the ceramide synthases CERS2-6 are regulated by phosphorylation in the C-terminal region. *J. Biol. Chem.* **291**, 7477–7487 (2016).
40. Hernandez-Corbacho, M. J. et al. Tumor necrosis factor-alpha (TNFα)-induced ceramide generation via ceramide synthases regulates loss of focal adhesion kinase (FAK) and programmed cell death. *J. Biol. Chem.* **290**, 25356–25373 (2015).
41. Mouton, R. E. & Venable, M. E. Ceramide induces expression of the senescence histochemical marker, β-galactosidase, in human fibroblasts. *Mech. Ageing Dev.* **113**, 169–181 (2000).
42. Limoges, M. A., Cloutier, M., Nandi, M., Ilangumaran, S. & Ramanathan, S. The GIMAP family proteins: an incomplete puzzle. *Front. Immunol.* **12**, 679739 (2021).

43. Prudent, R. & Cochet, C. New protein kinase CK2 inhibitors: jumping out of the catalytic box. *Chem. Biol.* **16**, 112–120 (2009).
44. Chen, Y. et al. Strategies of targeting CK2 in drug discovery: challenges, opportunities, and emerging prospects. *J. Med. Chem.* **66**, 2257–2281 (2023).
45. DeLeve, L. D. Liver sinusoidal endothelial cells in hepatic fibrosis. *Hepatology* **61**, 1740–1746 (2015).
46. Cogolludo, A., Villamor, E., Perez-Vizcaino, F. & Moreno, L. Ceramide and regulation of vascular tone. *Int. J. Mol. Sci.* **20**, 411 (2019).
47. Mittelbrunn, M. & Kroemer, G. Hallmarks of T cell aging. *Nat. Immunol.* **22**, 687–698 (2021).
48. O'Driscoll, M. et al. Age-specific mortality and immunity patterns of SARS-CoV-2. *Nature* **590**, 140–145 (2021).
49. Mellacheruvu, D. et al. The CRAPome: a contaminant repository for affinity purification-mass spectrometry data. *Nat. Methods* **10**, 730–736 (2013).

Publisher's note Springer Nature remains neutral with regard to jurisdictional claims in published maps and institutional affiliations.

This is a U.S. Government work and not under copyright protection in the US; foreign copyright protection may apply 2024, corrected publication 2024

Ann Y. Park[1,2,40], Michael Leney-Greene[1,2,3,40], Matthew Lynberg[1,2], Justin Q. Gabrielski[1,2], Xijin Xu[1,2], Benjamin Schwarz[4], Lixin Zheng[1,2], Arasu Balasubramaniyam[1,2,5], Hyoungjun Ham[2,3], Brittany Chao[1,2], Yu Zhang[2,3], Helen F. Matthews[1,2], Jing Cui[1,2], Yikun Yao[1,2], Satoshi Kubo[1,2], Jean Michel Chanchu[1,2], Aaron R. Morawski[1,2], Sarah A. Cook[1,2], Ping Jiang[1,2], Juan C. Ravell[1,2,6], Yan H. Cheng[1,2], Alex George[1,2], Aiman Faruqi[1,2], Alison M. Pagalilauan[1,2], Jenna R. E. Bergerson[3], Sundar Ganesan[7], Samuel D. Chauvin[1,2], Jahnavi Aluri[1,2], Joy Edwards-Hicks[8], Eric Bohrnsen[4], Caroline Tippett[9,10], Habib Omar[1,2], Leilei Xu[1,2], Geoffrey W. Butcher[11], John Pascall[11], Elif Karakoc-Aydiner[12,13], Ayca Kiykim[12], Holden Maecker[14], İlhan Tezcan[15], Saliha Esenboga[15], Raul Jimenez Heredia[16,17,18], Deniz Akata[19], Saban Tekin[20], Altan Kara[21], Zarife Kuloglu[22], Emel Unal[23], Tanıl Kendirli[24], Figen Dogu[25], Esra Karabiber[26], T. Prescott Atkinson[27], Claude Cochet[28], Odile Filhol[28], Catherine M. Bosio[4], Mark M. Davis[29], Richard P. Lifton[30,31], Erika L. Pearce[8,32], Oliver Daumke[5,33], Caner Aytekin[34], Gülseren Evirgen Şahin[35], Aysel Ünlüsoy Aksu[35], Gulbu Uzel[3], V. Koneti Rao[3], Sinan Sari[36], Buket Dalgıç[36], Kaan Boztug[16,17,18,37,38], Deniz Cagdas[15], Sule Haskologlu[25], Aydan Ikinciogullari[25], David Schwefel[5,33,39], Silvia Vilarinho[9,10], Safa Baris[12,13], Ahmet Ozen[12,13], Helen C. Su[2,3] & Michael J. Lenardo[1,2] ✉

[1]Molecular Development of the Immune System Section, Laboratory of Immune System Biology, National Institute of Allergy and Infectious Diseases, National Institutes of Health, Bethesda, MD, USA. [2]Clinical Genomics Program, National Institute of Allergy and Infectious Diseases, National Institutes of Health, Bethesda, MD, USA. [3]Laboratory of Clinical Immunology and Microbiology, National Institute of Allergy and Infectious Diseases, National Institutes of Health, Bethesda, MD, USA. [4]Laboratory of Bacteriology, National Institute of Allergy and Infectious Diseases, National Institutes of Health, Hamilton, MT, USA. [5]Department of Structural Biology, Max-Delbrück-Center for Molecular Medicine in the Helmholtz Association (MDC), Berlin, Germany. [6]Department of Internal Medicine, Hackensack Meridian School of Medicine, Nutley, NJ, USA. [7]Biological Imaging Section, National Institute of Allergy and Infectious Diseases, National Institutes of Health, Bethesda, MD, USA. [8]Department of Immunometabolism, Max Planck Institute of Immunobiology and Epigenetics, Freiburg, Germany. [9]Section of Digestive Diseases, Department of Internal Medicine, Yale School of Medicine, New Haven, CT, USA. [10]Department of Pathology, Yale School of Medicine, New Haven, CT, USA. [11]Laboratory of Lymphocyte Signaling and Development, The Babraham Institute, Cambridge, United Kingdom. [12]Division of Pediatric Allergy and Immunology, Marmara University, School of Medicine Pendik, Istanbul, Turkey. [13]The Isil Berat Barlan Center for Translational Medicine, Marmara University, Pendik, Istanbul, Turkey. [14]Institute for Immunity, Transplantation, and Infection, Stanford University School of Medicine, Palo Alto, CA, USA. [15]Department of Pediatrics, Division of Pediatric Immunology, Hacettepe University, Faculty of Medicine, Ankara, Turkey. [16]St Anna Children's Cancer Research Institute, Vienna, Austria. [17]Ludwig Boltzmann Institute for Rare and Undiagnosed Diseases, Vienna, Austria. [18]Department of Pediatrics and Adolescent Medicine, Medical University of Vienna, Vienna, Austria. [19]Department of Radiology, Faculty of Medicine, Hacettepe University, Ankara, Turkey. [20]Department of Basic Medical Sciences, Hamidiye Faculty of Medicine, Division of Medical Biology, University of Health Sciences, İstanbul, Turkey. [21]TUBITAK Marmara Research Center, Gene Engineering and Biotechnology Institute, Gebze, Turkey. [22]Department of Pediatrics, Division of Pediatric Gastroenterology, Hepatology, and Nutrition, Ankara University School of Medicine, Ankara, Türkiye. [23]Department of Pediatric Oncology, Ankara University Medical School, Ankara, Turkey. [24]Department of Pediatric Intensive Care Unit, Ankara University Medical School, Ankara, Turkey. [25]Department of Pediatric Immunology and Allergy, Ankara University Medical School, Ankara, Turkey. [26]Department of Chest Diseases, Faculty of Medicine, Division of Adult Allergy-Immunology, Marmara University, Istanbul, Turkey. [27]Department of Pediatrics, University of Alabama at Birmingham, Birmingham, AL, USA. [28]University Grenoble Alpes, INSERM, CEA, UMR Biosanté, Grenoble, France. [29]Institute for Immunity, Transplantation and Infection, Stanford University, Palo Alto, CA, USA. [30]Department of Genetics, Yale School of Medicine, Yale University, New Haven, CT, USA. [31]Laboratory of Human Genetics and Genomics, The Rockefeller University, New York, NY, USA. [32]The Bloomberg–Kimmel Institute for Cancer Immunotherapy at Johns Hopkins, Johns Hopkins University, Baltimore, MD, USA. [33]Institute for Chemistry and Biochemistry, Freie Universität Berlin, Berlin, Germany. [34]Department of Pediatric Immunology, Dr Sami Ulus Maternity and Children's Health and Diseases Training and Research Hospital, Ankara, Turkey. [35]Department of Pediatric Gastroenterology, Hepatology and Nutrition, University of Health Sciences, Dr Sami Ulus Maternity and Children's Health and Diseases Training and Research Hospital, Ankara, Turkey. [36]Department of Pediatric Gastroenterology, Gazi University Faculty of Medicine, Ankara, Turkey. [37]CeMM Research Center for Molecular Medicine of the Austrian Academy of Sciences, Vienna, Austria. [38]St Anna Children's Hospital, Vienna, Austria. [39]Bioanalytics Unit, Institute of Biotechnology, Technische Universität Berlin, Berlin, Germany. [40]These authors contributed equally: Ann Y. Park, Michael Leney-Greene. ✉e-mail: lenardo@nih.gov

Methods

Human participants

All enrolled participants provided written informed consent and samples were collected through approved protocols following local ethics and Institutional Review Board (IRB) policies. Patients P1.1–P1.6 (Age/Sex:17/M, 22/M, 34/F, 35/F, 44/M and 42/M) and patient P4.1 (10/M) were enrolled on National Institutes of Health (NIH) protocol 06-I-0015 (ClinicalTrials.gov NCT00246857). IRB approval was obtained from the NIH IRB on 16 February 2021. Patients P2.1–P2.2 (16/M, 23/M) were enrolled by Ankara University Faculty of Medicine Clinical Research Ethics Committee, approved 19 December 2020. Patients P3.1–P3.2 (26/F, 28/M) were enrolled using a protocol approved by Gazi University Ethics Committee 27 April 2020. Patient P5.1 (24/M) was enrolled on NIH Protocol 93-I-0063 (ClinicalTrials.gov NCT00001350). IRB approval was obtained from the NIH IRB on 14 April 2021. Patient P6.1 (23/M) was enrolled in NIH Protocol 93-I-01119 (ClinicalTrials.gov NCT00001355). IRB approval was obtained from the NIH IRB on 30 December 2020. Patient 7.1 (41/F) was enrolled by Hacettepe University Clinical Trials Ethics Committee, decision no. 2019/21-36 (KA-15069), approved on 19 December 2020. Patients P8.1 (18/M) and P9.1 (37/F) were approved by Marmara University Research Ethics Committee Document ID 70737436-050.01.04-E.2000065366, approved on 14 February 2020. Blood from healthy donors was obtained at the NIH Clinical Center under approved protocols.

Mice

All protocols were approved by the National Institute of Allergy and Infectious Diseases (NIAID) Animal Care and Use Committee and followed NIH and Department of Health and Human Services (HHS) guidelines. *Gimap5*$^{sph/sph}$ mice were a kind gift from K. Hoebe (Janssen Research and Development Spring House). Littermate C57BL/6 mice were used as WT controls. Sex-matched 4–12-week-old mice or aged (16–19-month-old) mice were used for all experiments. The 19-month-old C57BL/6 mice were purchased from Charles River Laboratories.

Primary T cell culture

Human peripheral blood mononuclear cells (PBMCs) were isolated by Ficoll-Paque PLUS (GE Healthcare) density gradient centrifugation, washed twice in phosphate-buffered saline (PBS) and resuspended at 10^6 ml^{-1} in complete RPMI 1640 (cRPMI) medium containing 10% fetal bovine serum, 2 mM glutamine and 100 U ml^{-1} each of penicillin and streptomycin (Invitrogen). Cells were activated with 1 µg ml^{-1} anti-CD3 (clone HIT3α, BioLegend) and 1 µg ml^{-1} anti-CD28 (clone CD28.2, BioLegend) or with Dynabeads Human T-Activator CD3/CD28 (Thermo Fisher Scientific). After 3 d, activated T cells were washed and cultured in cRPMI with 100 U ml^{-1} recombinant human IL-2 (rhIL-2, R&D). For patient cells, freshly isolated or frozen PBMCs were stimulated at 5×10^6 ml^{-1} in cRPMI with 2 µg ml^{-1} of phytohemagglutinin-L (Sigma-Aldrich), in the presence of 1 µg ml^{-1} anti-CD28 and 1 ng ml^{-1} recombinant IL-7 (BioLegend) for 48 h. The cells were washed twice with cRPMI and resuspended in medium at 10^6 ml^{-1} with 100 IU ml^{-1} rhIL-2 and cultured for up to 3 weeks with fresh IL-2 and medium supplemented every 2 d. Murine T lymphocytes were prepared from lymph nodes or spleen, treated with 5 µg ml^{-1} concanavalin A (Sigma) for 48 h followed by washing with 10 mg ml^{-1} of α-methylmannoside (Sigma). The activated cells were supplemented with fresh IL-2 and medium every 2 d.

CRISPR/Cas9-mediated gene knockout in primary T cells

Each crRNA and tracrRNA (Integrated DNA Technologies, cat. no. 1073191) were reconstituted to 100 µM with Nuclease-Free Duplex Buffer (Integrated DNA Technologies) and mixed at equimolar concentrations in a sterile PCR tube. Mixed oligonucleotides were annealed by heating at 95 °C for 5 min in PCR thermocycler. After cooling of complexes to 23 °C, 9 µl three crRNAs–tracrRNA complexes (3 µl equal to 150 pmol each), 4.5 µl Cas9 protein (30 µg per 180 pmol, MacroLab Facility) and 1.5 µl nuclease-free duplex buffer were gently triturated and incubated at 23 °C for 10 min. Then, 10×10^6 purified resting primary human T cells or 30×10^6 murine T cell blasts were resuspended in 20 µl of P2 buffer (P2 Primary Cell 4D-NucleofectorTM X kit L, Lonza) or 60 µl P4 buffer (P4 Primary Cell 4D-NucleofectorTM X kit L, Lonza), respectively. T cells were transferred to sterile PCR tubes containing the crRNAs–tracrRNA–Cas9 complexes (RNP), mixed and transferred to nucleofection cuvettes (4D-Nucleofector X kit L, Lonza). T cells were electroporated using a 4D-Nucleofector (Lonza). EH100 program was used for resting human T cells and CM137 program was used for murine T cell blasts. After nucleofection, T cells were transferred to six-well plates containing cRPMI for resting T cells or cRPMI with IL-2 for T cell blasts. Dead cells were removed by dead cell removal kit (Miltenyi Biotec) after 24 h. Transfection efficiency exceeding 90% was confirmed by assessing a fluorescently tagged crRNA control (IDT, cat. no. 1077024) after 24 h. Murine T cells tend to die within 24–48 h in vitro when not activated[50,51], so murine T cells were activated before RNP/gRNA transfection for better viability and efficiency as previously reported[30]. Notably, RNP/gRNA electroporation in unstimulated human primary T cells yielded substantial KO efficiency, without apparent impact on T cell activation or subpopulation composition. Oligonucleotide sequences are provided as Supplementary Data 1.

Electron microscopy

For transmission electron microscopy, murine T cell blasts were fixed in 500 µl 3% paraformaldehyde + 0.35% glutaraldehyde in 0.1 M sodium cacodylate buffer pH 7.4 (Electron Microscopy Sciences). Samples were processed in the microwave (Biowave Pro, Pelco) as follows. Samples were post-fixed with 0.5% osmium tetroxide + 0.8% potassium ferrocyanide in 0.1 M sodium cacodylate buffer for 2 cycles (2 min on, 2 min off then 2 min on), rinsed for 45 s in buffer and then processed for two cycles (2 min on, 2 min off then 2 min on) in aqueous 1% tannic acid, rinsed for 45 s in distilled water, then processed for two cycles (2 min on, 2 min off then 2 min on) in aqueous 1% samarium acetate and rinsed for 45 s in distilled water. Samples were dehydrated in a graded ethanol series for 45 s at each step and embedded in epon/araldite (Electron Microscopy Sciences). The 70-nm sections were imaged on a Hitachi 7800 transmission electron microscope operating at 80 kV.

For scanning electron microscopy, 5×10^6 murine T cell blasts were fixed in 2% paraformaldehyde in 0.1 M sodium cacodylate buffer (Electron Microscopy Sciences). Cells were settled for 1.5 h on silicon chips treated with sticky acetone and glow-discharged, then rinsed with 0.1 M sodium cacodylate buffer. Samples were post-fixed for 2 h in 0.5% osmium tetroxide + 0.8% potassium ferrocyanide in 0.1 M sodium cacodylate buffer, then rinsed in distilled water. Samples were taken through a graded dehydration series with ethanol, critical point dried (CPD 030, Baltec), then coated with iridium (300TD, Electron Microscopy Sciences). Images were acquired on a Hitachi SU8000 scanning electron microscope operating at 5 kV.

Lipid sample preparation and liquid chromatography–mass spectrometry

Only liquid chromatography–MS (LC–MS) grade solvents were used. Cell culture samples (≥500,000 cells per sample) were fixed in 0.5 ml ice-cold methanol for 5 min. Then, 0.5 ml ice-cold water followed by 0.5 ml ice-cold chloroform were then added. Samples were shaken for 30 min at 4 °C and then centrifuged at 16,000*g* for 20 min. Then, 400 µl of the top (aqueous) layer and bottom (organic layer) were collected. The aqueous layer was directly prepared for LC–MS injection. The organic layer was dried in a speedvac and stored at −80 °C until analysis at which time samples were resuspended in 1 ml 5 µg ml^{-1} butylated hydroxytoluene in 6:1 isopropanol:methanol.

For LC–MS, tributylamine and all synthetic molecular references were obtained from Millipore Sigma. Aqueous metabolite and lipid samples were analyzed using targeted multiple-reaction monitoring (MRM) methods. Separations used a Sciex ExionLC AC system and analyzed using a Sciex 5500 QTRAP mass spectrometer. Injection order was randomized and quality control and blank injections were interspersed throughout the runs. Aqueous metabolites were analyzed using a previously established ion pairing method with modification. Samples were separated on a Waters Atlantis T3 column (100 Å, 3 µm, 3 mm × 100 mm) and eluted using a binary gradient from 5 mM tributylamine, 5 mM acetic acid in 2% isopropanol, 5% methanol, 93% water (v/v) to 100% isopropanol over 15 min. Analytes were detected in negative mode using two distinct MRM pairs for each metabolite when possible. Heavy labeled standards were not utilized and only relative quantification was performed. Lipid samples were analyzed using a previously established hydrophilic interaction liquid chromatography (HILIC) method with modification. Samples were separated on a Water XBridge Amide column (3.5 µm, 3 mm × 100 mm) and eluted using a 12-min binary gradient from 100% 5 mM ammonium acetate, 5% water in acetonitrile apparent pH 8.4 to 95% 5 mM ammonium acetate, 50% water in acetonitrile at pH 8.0. Target lipids were detected using scheduled MRM. Lipid signals were analyzed by either negative mode or positive mode with separate injections. All signals were integrated using MultiQuant Software v.3.0.3. Signals with greater than 50% missing values were discarded and the remaining missing values were replaced with the lowest registered signal value. Additionally, lipids with a quality control coefficient of variance over 30% were discarded. We used total sum normalization independently for the lipid-positive and -negative and aqueous metabolites datasets. Datasets were combined and each signal was indexed. Aqueous metabolite data were filtered to remove features with missing values in over 50% of samples. Initial analysis was performed with multiple MRM signals included for each metabolite when possible. For display and pathway mapping, a single MRM signal was used for each metabolite. Single and multivariate analysis was performed in MarkerView Software v.1.3.1 except for ANOVA analysis, which was performed using MetaboAnalyst 3.0 For partial least squared discriminant analysis, samples were Pareto scaled. For heat map displays, signals were auto-scaled.

For Fig. 4d, we used biphasic methyl tert-butyl ether (MTBE) extraction. In brief, cells were resuspended in 100 µl cold PBS in glass vials. Cold methanol (750 µl), MTBE (2 ml) and water (625 µl) were added sequentially with vortexing. Phases were separated by centrifugation and the upper organic phase was dried and resuspended in 2:1:1 isopropanol:acetonitrile:water before analysis. LC–MS used an Agilent Zorbax Eclipse Plus C18 column using an Agilent 1290 Infinity II UHPLC in line with an Agilent 6495 Triple Quad QQQ-MS. Lipids were identified and quantified using Agilent Mass Hunter software (B.08.02). *P* values for lipid chromatography heat map figures are provided as Supplementary Data 2.

Flow cytometry

For surface staining, PBMCs and T cell blasts were washed in fluorescence activated cell sorting (FACS) buffer (PBS containing 5% FBS and 0.1% NaN_3) and stained in 50 µl FACS buffer containing indicated fluorochrome-labeled antibodies (1:100 dilution) for 30 min on ice. Cells were then washed three times in FACS buffer and fixed before acquisition on either a LSR II or LSRFortessa (BD Biosciences). For viability analyses, PBMCs and T cell blasts were stained with Zombie Aqua (BioLegend, 1:500 dilution). Mouse ECs were prepared from mice liver and lung using the Multi Tissue Dissociation kit 2 (Miltenyi Biotec). The liver was collected after PBS perfusion and collagenase digestion and then cells were enriched by Percoll density centrifugation as previously described[9]. For intracellular staining, cells were fixed and permeabilized with BD Cytofix/Cytoperm solution for 20 min at 4 °C and then washed twice in BD Perm/Wash buffer. Cells were then incubated in BD Perm/Wash buffer containing fluorochrome-conjugated antibodies for 30 min at 4 °C in the dark. The following dilutions were used for mouse T cell intracellular staining: anti-p53-FITC (BD Bioscience, 1:15 dilution), anti-p16 (Thermo Fisher Scientific, 1:200 dilution) and Alexa Fluor 647 anti-p21 (Abcam, 1:500 dilution). For human T cells, Alexa Fluor 594 anti-p53 (BioLegend,1:100 dilution), Alexa Fluor 647 anti-p16 (Cell Signaling Technology, 1:50 dilution), and Alexa Fluor 488 anti-p21 (Cell Signaling Technology, 1:50 dilution) were used. For SA-β-gal activity, CellEvent Senescence Green Detection kit was used following the manufacturer's protocol (Thermo Fisher Scientific, C10850). Cells were washed twice with BD Perm/Wash buffer, once with FACS buffer and resuspended in FACS buffer before acquisition. For mouse p21 staining, cells were fixed with 80% methanol for 5 min and permeabilized with 0.1% Triton X-100 in PBS for 15 min. Cells were then blocked with 10% goat serum in 1× PBS for 30 min and incubated with Alexa Fluor 647 anti-p21 for 30 min at room temperature. Cells were washed three times in FACS buffer before acquisition. Data were analyzed using FlowJo v.10.5.3. and v.10.8.0. A figure depicting the gating strategies can be found in the Supplementary Information (Supplementary Fig. 1).

Exome and whole-genome sequencing analysis

Genomic DNA was isolated from PBMCs and whole-exome sequencing or whole-genome sequencing (WGS) was performed using SureSelect Human All Exon 50 Mb kit (Agilent Technologies) and the Illumina HiSeq sequencing system (Illumina), respectively, with analysis using the Standard Coverage Human WGS from the Broad Institute. Whole-exome sequencing produced ~50–100× sequence coverage for targeted regions and WGS produced 60× coverage for proband and 30× coverage for family members. DNA sequences were aligned to the reference human genome (build 19) using Burrows–Wheeler Aligner with default parameters and variants were called using the Genome Analysis ToolKit. Variants were then annotated by functional impacts on encoded proteins and prioritized based on the genetic model and minor allele population frequency (MAF). Autosomal-recessive inheritance was investigated for genes with rare homozygous or compound heterozygous recessive variants with MAF < 1% from gnomAD.

CyTOF

This assay was performed with the Human Immune Monitoring Center at Stanford University as previously described[27]. Frozen PBMCs from two patients (P1.1 and P1.4) or healthy controls were thawed, washed twice, resuspended in CyFACS buffer (PBS supplemented with 2% BSA, 2 mM EDTA and 0.1% NaN_3) and viable cells were counted by Vicell (Beckman Coulter). Then, 1.5×10^6 viable cells were stained for 60 min on ice with 50 ml antibody–polymer conjugate cocktail, described in Supplementary Table 5. Sources for antibodies are listed in Supplementary Table 5 and the polymer and metal isotopes were purchased from Fluidigm. Washed cells were treated with 2 mg ml^{-1} LiveDead (DOTA-maleimide (Macrocyclics) containing natural-abundance indium), fixed with 2% paraformaldehyde in PBS and placed at 4 °C overnight. Cells were pelleted and washed in PBS, then washed in MilliQ water before resuspension in 700 µl MilliQ water before injection into the CyTOF (Fluidigm). Data analysis used FlowJo v.9.3 (CyTOF settings) by gating on intact cells based on the iridium isotopes from the intercalator, then on singlets by Ir-191 versus cell length and then on live cells (Indium-LiveDead minus population). Population analysis was carried out using SPADE v.3.9 with the following definitions:

T cells, $CD3^+CD19^-CD33^-$
$CD4^+$ T cells, $CD4^+CD8^-TCR\gamma\delta^-$
$CD8^+$ T cells, $CD8^+CD4^-TCR\gamma\delta^-$
$TCR\gamma\delta$ T cells, $CD3^+TCR\gamma\delta^+$
Naive T cells, $CD45RA^+CCR7^+$
T_{EM} cells, $CD45RA^-CCR7^-$

T_{CM} cells, $CD45RA^{-}CCR7^{+}$
$CD45RA^{+}$ T_{EMRA} cells, $CD45RA^{+}CCR7^{-}$
NK cells, $CD56^{+}HLA\text{-}DR^{-}CD3^{-}CD19^{-}CD33^{-}$
B cells, $CD19^{+}CD20^{+}CD3^{-}CD33^{-}$

Telomere analysis
Frozen PBMCs from patient P1.3 and P1.4 were analyzed by Repeat Diagnostics for measurement of telomere length via Flow-FISH. Signal strength was then plotted relative to telomere lengths for healthy controls to calculate the percentile for each patient.

Orthologs and other human GIMAPs
FL orthologs of GIMAP5 protein sequences from several species and related human GIMAP family members (GIMAP1, 2, 4, 6, 7 and 8) were obtained from GenBank. Protein sequences were aligned using the Clustal Omega algorithm.

GIMAP5 purification
A construct encoding human GIMAP5 amino acids 1 to 276 ($GIMAP5^{1-276}$) was cloned into the pGEX-6P-1 plasmid (GE Healthcare) with an N-terminal GST tag and grown in *Escherichia coli* Rosetta 2DE3 strain (Novagen). *E. coli* cells expressing $GIMAP5^{1-276}$ were grown to an optical density of 0.6 and induced with 40 µM IPTG at 18 °C overnight. Cells were pelleted at 2,392*g* at 4 °C for 15 min and resuspended in lysis buffer (50 mM HEPES, pH 7.5, 800 mM NaCl, 2.5 mM dithiothreitol, 10 mM KCl, 1 mM ATP, 0.1 mM Pefabloc protease inhibitor and 1 µM DNase I). The cells were ruptured using a Microfluidizer (Microfluidics) and the lysate was centrifuged at 51,275*g* at 4 °C for 45 min. Filtered supernatant from the cleared lysate was applied on a chromatography column packed with 20 ml GSH Sepharose beads (Sigma, GE17-0756-01) pre-equilibrated with five column volumes (CVs) buffer 1 (50 mM HEPES, pH 7.5, 800 mM NaCl, 2.5 mM dithiothreitol, 10 mM KCl and 1 mM ATP). All the chromatographic procedures were carried out at 4 °C. The column was washed with 20 × CVs of buffer 1 until the E280 signal reached baseline. Subsequently, the column was washed with 10 × CVs buffer 2 (50 mM HEPES, pH 7.5, 800 mM NaCl, 2.5 mM dithiothreitol, 10 mM KCl, 1 mM ATP and 10 mM EDTA) followed by 5 × CVs buffer 1 to remove partially bound nucleotides. For purification of GST-fusion, the protein was eluted with 50 ml buffer 3 (50 mM HEPES, pH 7.5, 500 mM NaCl, 2.5 mM dithiothreitol and 20 mM glutathione, pH readjusted to 7.5). To remove the GST affinity tag, if applicable, GSH Sepharose beads were removed from the columns and resuspended in 40 ml buffer 1. Then, 0.5 mg preScission protease was added and the beads were incubated overnight at 4 °C under rotation. After incubation, GSH Sepharose beads were filled into the chromatography column and the cleaved protein was eluted with 2 × CVs of buffer 1. Eluates were concentrated using Amicon centrifugal filter devices (Merck) to a volume of 1–5 ml. Concentrated samples were applied to a Superdex 200 column pre-equilibrated with buffer 5 (10 mM HEPES, pH 7.5, 300 mM NaCl and 2.5 mM dithiothreitol). Fractions were analyzed on SDS–PAGE, pooled and concentrated to 20 mg ml^{-1}. Protein concentration was measured at 280 nm and aliquots were snap-frozen in liquid nitrogen and stored at −80 °C.

Protein thermal shift assay
Protein unfolding was monitored by Protein Thermal Shift Dye (Applied Biosystems) fluorescence on a Bio-Rad CFX96 RT–PCR machine in temperature increments of 0.5 °C min^{-1}. Reactions were prepared according to the manufacturer's protocol (Protein Thermal Shift Dye kit). Purified GST (25 µM), $GST\text{-}GIMAP5^{WT}$ (50 µM), $GST\text{-}GIMAP5^{L223F}$ (50 µM), $GST\text{-}GIMAP5^{I47T}$ (50 µM), $GST\text{-}GIMAP5^{L204P}$ (50 µM) and $GST\text{-}GIMAP5^{N221S}$ (50 µM) were heated from 25 °C to 80 °C in a buffer containing 10 mM HEPES, pH 7.5, 450 mM NaCl, 2.5 mM dithiothreitol, 100 µm GTP and 5 mM $MgCl_2$. Each reaction was carried out in a 20-µl volume in triplicate in a 96-well plate.

Crystallization
Nucleotide-free protein was diluted to 15 mg ml^{-1} with protein buffer (10 mM HEPES, pH 7.5, 150 mM NaCl, 2.5 mM dithiothreitol, 2 mM $MgCl_2$ and 2 mM GDP; Jena Bioscience). Crystallization in hanging drop vapor-diffusion yielded clusters of small plate-like crystals from mixing equal volumes (1 µl) of protein solution and a reservoir solution (500 µl) containing 16% 2-propanol and 50 mM ammonium citrate. A single plate (50 × 50 × 5 µm) was broken off and frozen after transfer to a solution containing 10 mM HEPES, pH 7.5, 150 mM NaCl, 2.5 mM dithiothreitol, 2 mM $MgCl_2$, 2 mM GDP, 16% 2-propanol, 50 mM ammonium citrate and 20% glycerol by plunging it into liquid nitrogen.

Data collection, structure solution, refinement and structure analysis
Datasets from single crystals were recorded using the rotation method with a φ increment of 1° at a temperature of −173 °C on a BESSY II beamline 14.1 with a Rayonics MX 225 CCD detector. Recorded intensities were integrated and scaled with the program XDS[52]. The structure was solved by molecular replacement using the program MOLREP with the structure of nucleotide-free GIMAP2 residues 1–260 as template (Protein Data Bank (PDB) code 2XTP)[53] and fitted into electron density maps using the program Coot[54] refined with Refmac5. Standard positional refinement has been applied, preceded by TLS (translational, libration, screw rotation displacement) refinement. Then, 5% of measured reflections were set aside for cross-validation. The final model consists of GIMAP5 residues 27–263, 94% of the residues are in the favored region of the Ramachandran plot and 0.4% are outliers, as determined by MolProbity[55]. Data collection and refinement statistics are shown in Supplementary Table 4. Structure representations were prepared using PyMOL (The PyMOL Molecular Graphics System, v.1.7.6.2 Schrödinger). Structural superpositions were computed using the protein structure comparison service PDBeFold at European Bioinformatics Institute (www.ebi.ac.uk/msd-srv/ssm)[56].

scRNA-seq
Publicly available single-cell RNA sequencing (scRNA-seq) raw count data from PBMCs were acquired from the 10x Genomics data repository (support.10xgenomics.com/single-cell-gene-expression/datasets). Then, 3,000 PBMCs from a healthy donor dataset were analyzed using Seurat in R studio v.4.0.0, log-normalized and scaled using default settings. The cells were grouped using *k*-nearest neighbors on the top 12 dimensions from principal-component analysis and clustered using the Louvain algorithm with a resolution of 0.5. The clusters were projected into a two-dimensional space using Uniform Manifold Approximation and Projection and identified using canonical markers.

Immunoblotting
Cell pellets were incubated for 15 min in lysis buffer (1% NP-40, 150 mM sodium chloride, 50 mM Tris-HCl, pH 7.4 plus Halt Protease and Phosphatase Inhibitor Cocktail) and then clarified via centrifugation at 14,000 to 16,000*g* at 4 °C for 15 min. For mice organs, the spleen, liver, lung, heart, kidney and brain were collected after PBS perfusion and dissociated into single-cell suspensions using homogenizer (MP Biomedicals) in RIPA buffer (Thermo Scientific). Total protein levels were measured by BCA assay (Thermo Scientific) before reduction with 5% β-mercaptoethanol and SDS Loading Solution (Quality Biological) at 95 °C for 10 min. Equal protein amounts were electrophoresed on either 4–12% or 10% Bis-Tris gels (NuPAGE, Life Technologies) and wet-transferred to nitrocellulose membranes that were blocked in 5% non-fat milk in TBST (0.05% Tween-20) and probed with primary antibodies. The following antibodies were used: GIMAP1 (MAC451, 1:1,000 dilution), GIMAP4 (MAC426, 1:1,000 dilution), GIMAP5 (MAC429, 1:1,000 dilution)[12], GIMAP6 (MAC445, 1:1,000 dilution)[57], GIMAP7 (MAC453, 1:1,000 dilution) and Gimap5 (MAC421, 1:1,000 dilution)[12] or GIMAP2 (1:1,000

dilution) and GIMAP8 (1:1,000 dilution), produced by GenScript. β-Actin (Abcam, 1:1,000 dilution), β-tubulin (Cell Signaling Technology, 1:1,000 dilution), HSP90 (Cell Signaling Technology, 1:1,000 dilution), p21 (Cell Signaling Technology, 1:1,000 dilution), p53 (Millipore, 1:1,000 dilution), p16 (Cell Signaling Technology, 1:1,000 dilution), c-myc (Cell Signaling Technology, 1:1,000 dilution), LCK (BioLegend, 1:1,000 dilution), CERS2 (Invitrogen, 1:1,000 dilution), CK2B (Proteintech, 1:1,000 dilution), CK2A1 (Proteintech, 1:1,000 dilution), phospho-p44/42 MAPK (Erk1/2) (Thr202/Tyr204) (pERK, Cell Signaling Technology, 1:1,000 dilution), phospho-p70 S6 kinase (Thr421/Ser424) (pS6K, Cell Signaling Technology, 1:1,000 dilution), GFP (Cell Signaling Technology, 1:1,000 dilution), HA (Cell Signaling Technology, 1:1,000 dilution), Flag (Cell Signaling Technology, 1:1,000 dilution) and Flag (BioLegend, 1:1,000 dilution). Binding of primary antibodies was then measured via HRP-tagged antibodies specific for the relevant species (Southern Biotech, 1:2,000 dilution) and visualized by chemiluminescent substrates (Immobilon Classico/Forte western HRP substrate, Thermo Fisher SuperSignal West Femto Maximum Sensitivity Substrate or Thermo Fisher SuperSignal West Dura Extended Duration Substrate).

Proliferation assay

Healthy donor and patient T cells were labeled with CellTrace Violet dye (Thermo Fisher Scientific) for 20 min at room temperature, centrifuged and resuspended in cRPMI with anti-CD3 (HIT3α, BioLegend) and anti-CD28 (CD28.2, BioLegend) or with Dynabeads Human T-Activator CD3/CD28 (Thermo Fisher Scientific). After 72 h stimulation, cells were analyzed via flow cytometry.

Cell cycle analysis

Cells were labeled with 5 µM of Vybrant DyeCycle Stain (Thermo Fisher Scientific) at 37 °C in the dark for 30 min and analyzed by flow cytometry. Cell cycle distribution was quantified using FlowJo v.10.6.2 software.

GST pulldown assay and mass spectrometry

Purified GST and GST-GIMAP5^{wt} proteins (100 µg) were immobilized on glutathione agarose (Thermo Fisher Scientific) in binding buffer (25 mM HEPES, pH 7.3, 1 mM EDTA and 5 mg ml^{-1} BSA) with rotation for 45 min at 4 °C. GDP (500 µM) or GTPγS (500 µM) was loaded in GST or GST-GIMAP5^{wt}-bound glutathione agarose for 15 min at 30 °C under agitation to analyze the interaction with the GDP- or GTP- bound form of GIMAP5. The reaction was stopped by adding 20 mM $MgCl_2$. Jurkat cells (ATCC, cat. no. TIB-152) were lysed in lysis buffer (0.5% NP-40, 25 mM HEPES, pH 7.3, 25 mM NaCl, 1 mM EDTA and 0.5 mM $CaCl_2$) and 2.5 mg of lysates per sample were incubated with GTPγS-charged GST and GST-GIMAP5 and GDP-charged GST-GIMAP5^{wt}-bound glutathione agarose at 4 °C for 90 min. The bound complexes were eluted in 100 µl elution buffer after washing the beads four times with lysis buffer. Twenty percent of the eluted samples were assayed by GIMAP5 immunoblot to confirm the GST pulldown and the rest of eluted samples were submitted to the NIDDK/NIH Mass Spectrometry Core for analysis. Biological samples were analyzed in triplicate by stripping the protein components off the beads using sodium laurate, creating a tryptic digest, incorporating different isotopes using reductive dimethylation, pooling samples and then performing LC–MS/MS. The resulting data were analyzed using MaxQuant v.1.66 using default settings searched against the human proteome, control proteins and known contaminants.

Co-immunoprecipitation

The 2×10^7 cycling primary T cell blasts were incubated with cRPMI containing 0.5 IU ml^{-1} (U ml^{-1}) IL-2 overnight and restimulated with HIT3α (BioLegend, 10 µg ml^{-1}) and F(ab')$_2$ fragment goat anti-mouse IgG (Jackson ImmunoResearch, 10 µg ml^{-1}) for human T cells or with immobilized anti-CD3 and anti-CD28 (2 µg ml^{-1} each) for murine T cells. Cell lysates were precleared with unconjugated Dynabeads Protein G (Thermo Fisher Scientific) rotated for 30 min with rotation at 4 °C. Primary antibodies were then added to the precleared lysates and rotated overnight at 4 °C. Dynabeads Protein G were added and incubated for an additional 1 h at 4 °C. For transfections, cell lysates were rotated with Flag-Dynabeads Protein G complex for 1 h at 4 °C. Immunoprecipitates were washed four times with lysis buffer and eluted from the Dynabeads via 5 min at 95 °C in SDS sample loading buffer followed by electrophoresis and immunoblotting.

Transfection. HEK293T cells (ATCC, cat. no. CRL-3216) were seeded to 70% density in cDMEM. Tagged plasmids were diluted in Opti-MEM reduced serum medium (Thermo Fisher Scientific) and combined with Lipofectamine 3000 Transfection Reagent (Thermo Fisher Scientific, cat. no. L3000075) for transfection according to the manufacturer's instructions. Cell lysates were made 24 h later for co-immunoprecipitation. FL GIMAP5, truncation mutants of GIMAP5 and GFP were cloned into the pCI-neo plasmid (Promega). CK2A1-HA, CK2A2-HA and CK2B-myc plasmids were purchased from Addgene.

Proximity ligation assay

Primary human T cells were plated onto poly-L-lysine coated coverslips for 5 min and fixed with 4% paraformaldehyde for 15 min at 23 °C. After washing twice with PBS, the samples were permeabilized for 15 min using 0.1% Triton X-100 at room temperature, washed twice with PBS and resuspended in 1 ml Duolink blocking solution for 1 h. Cells were washed twice with PBS and resuspended in 50 µl specified primary antibody solutions overnight with shaking at 4 °C. The following morning, cells were washed twice in Duolink Buffer A, then incubated in secondary antibody for 1 h at 37 °C. Samples were sequentially washed twice, incubated with ligase for 30 min at 37 °C, washed twice and incubated with Duolink In Situ Detection Reagents Green (Sigma-Aldrich) at 37 °C for 2 h. Cells were then washed twice and either analyzed by flow cytometry or mounted on glass slides in Prolong Antifade with 4,6-diamidino-2-phenylindole (Life Technologies, P36971) for acquisition with a Leica SP5 X-WLL microscope.

Confocal microscopy

Cells were plated onto poly-L-lysine-coated coverslips for 5 min and fixed with 4% paraformaldehyde for 15 min at room temperature. After washing twice with PBS, the samples were permeabilized for 15 min using 0.1% Triton X-100 at room temperature, washed twice with PBS and then blocked with 5% BSA in PBS with 0.05% Tween-20 for at least 45 min at room temperature. Samples were then incubated with primary antibodies diluted in PBS with 0.05% Tween-20 and 5% BSA overnight at 4 °C. The following primary antibody dilutions were used: anti-GIMAP5 (MAC429, 1:1,000 dilution), anti-CK2α (Proteintech, 1:100 dilution), anti-CK2α (Sigma, 1:100 dilution), anti-LCK (BioLegend, 1:75 dilution), anti-LAMTOR4 (Cell Signaling Technology, 1:500 dilution), anti-LAMP1 (Cell Signaling Technology, 1:100 dilution), anti-Rab7 (Cell Signaling Technology, 1:100 dilution), anti-calnexin (Cell Signaling Technology, 1:100 dilution) and anti-calnexin (BioLegend, 1:400 dilution). After washing twice, the samples were then treated with Alexa Fluor-conjugated secondary antibodies (Thermo Fisher Scientific, 1:400 dilution) for 30 min at 23 °C in the dark. Following two washes with PBS, then coverslips were mounted with Prolong Antifade with 4,6-diamidino-2-phenylindole (Life Technologies, P36971) onto slides and left to dry overnight. For MitoTracker staining, cycling T lymphocytes were incubated for 30 min at 37 °C with 6.25 nM of MitoTracker Red CMX-ROS (Invitrogen, M7521) in complete RPMI with 100 U ml^{-1} IL-2. Confocal images were acquired on a Leica SP8 WLL FLIM microscope and for STED, images were acquired using a Leica SP8 STED microscope. Analysis was performed using Imaris software.

Lentivirus production, transduction and cell purification

Lentivirus production and transduction were performed in human T cells as previously described[58]. Briefly, Lenti-X 293T cells (Takara, cat. no. 632180) were transfected with a third-generation lentivirus backbone (psPAX2, pMD2.G) and the plasmid of interest (pLV-EF1α-IRES-PuroR or pLV-EF1α-GIMAP5-IRES-PuroR) using Lipofectamine 3000 reagent. Lentivirus-containing supernatants were collected 48 and 72 h after transfection. The supernatants were clarified after centrifugation (500*g*, 15 min, 4 °C), combined with Lenti-X Concentrator (Takara, cat. no. 631232) and incubated at 4 °C overnight after gentle inversion. Virus was pelleted by centrifugation (1,500*g*, 45 min, 4 °C) and the pellet was gently resuspended in 1:20 of the original volume using complete RPMI medium. Human PBMCs were isolated as described above, further depleted with the Pan T Cell Isolation kit (Miltenyi Biotec) and activated with Dynabeads Human T-Activator CD3/CD28. After 24 h, T cells were transduced by resuspension to 5×10^5 cells ml^{-1} in cRPMI with 100 U ml^{-1} rhIL-2, 10 µg ml^{-1} of polybrene and 100 µl concentrated viral supernatant per 5×10^5 cells, followed by centrifugation (800*g*, 90 min, 37 °C). Then, 72 h after transduction, cells were purified by resuspension in cRPMI with 1 µg ml^{-1} of puromycin for 72 h.

Mouse retrovirus production, transduction and cell purification

Platinum-E cells (Cell Biolabs, cat. no. RV-101) were grown to 70% confluence and transfected with the packaging plasmid pCL-Eco along with the plasmid of interest (GFP-EV, GFP-T2A-Gimap5(WT), GFP-T2A-R121D, GFP-T2A-S40N) cloned into the pMSGV1 vector. Cell culture medium was replaced the following day and the viral supernatant was collected approximately 48 h after transfection. The supernatants were clarified by centrifugation (500*g*, 15 min, 4 °C), combined with Retro-X concentrator (Takara, cat. no. 631455) and incubated at 4 °C overnight after gentle inversion. Virus was pelleted by centrifugation (1,500*g*, 45 min, 4 °C) and the pellet was gently resuspended in 1:20 of the original volume using complete DMEM. *Sphinx* CD4$^+$ T lymphocytes were prepared from lymph nodes or spleen with the consecutive negative and positive isolations (Miltenyi Biotec) and activated with plate-bound IgG (Sigma-Aldrich cat. no. SAB3700455) + soluble 2 µg ml^{-1} CD3 and CD28 (BioLegend, cat. nos. 100340 and 102102). After 24 h, T cells were transduced by resuspension to 0.5 million cells per ml in cRPMI with 100 U ml^{-1} rhIL-2, 10 µg ml polybrene and 500 µl concentrated viral supernatant per 5×10^5 cells, followed by centrifugation (800*g*, 90 min, 37 °C). Similarly, NIH-3T3 (ATCC, cat. no. CRL-1658) cells were transduced with 50–100 µl per 0.5 million cells. Note that NIH-3T3 cells lack endogenous Gimap5 protein and T2A containing constructs migrate more slowly than GFP (Extended Data Fig. 4e).

Blinding, study design and statistical analyses

The sample size of 3–15 per group were used for in vitro and in vivo studies. These numbers were chosen based on hundreds of experiments in our laboratory[59–61]. Investigators were blinded wherever possible during sample analysis by coding sample identity during data collection for mice experiment and confocal experimentation (Fig. 3 and Extended Data Figs. 3 and 7). Else, blinding was not possible as the same investigator performed experiments and data analytics. Allocation of WT and mutant mice was random in Fig. 3 and Extended Data Figs. 3 and 4. For all other experiments, randomization was not conducted because experiments either compared individuals with and without the loss-of-function mutations or were sampled from a cell suspension for treatment/evaluation. No data were excluded. Data were analyzed using GraphPad Prism v.8.0 using a two-tailed unpaired, paired Student's *t*-test or by two-way ANOVA with Bonferroni post-test. *P* values < 0.05 were considered significant, whereas *P* values > 0.05 were considered non-significant. Flow cytometry data were analyzed via FlowJo v.10.6.2 (TreeStar). No statistical methods were used to predetermine sample size. Details on the test used can be found in the respective figure legends. Data distribution was assumed to be normal but this was not formally tested.

Limitations of the study

The limitations of this study are that the experimental analysis was constrained by the availability and health status of participants and their families. Due to these factors, the sample size may have been smaller than desired.

Reporting summary

Further information on research design is available in the Nature Portfolio Reporting Summary linked to this article.

Data availability

The human exome and genome sequencing data reported in this paper are deposited in dbGaP as phs002816.v1.p1. The coordinates and structure factors for the crystal structure have been deposited at the PDB with the accession code 6Z3E (the validation report can be found online). Database/datasets used are PDB 2XTP, 2XTO and 3ZJC and 10x Genomics, 3k PBMCs from a healthy donor (www.10xgenomics.com/resources/datasets/3-k-pbm-cs-from-a-healthy-donor-1-standard-1-1-0). Source data are provided with this paper.

References

50. Vella, A., Teague, T. K., Ihle, J., Kappler, J. & Marrack, P. Interleukin 4 (IL-4) or IL-7 prevents the death of resting T cells: stat6 is probably not required for the effect of IL-4. *J. Exp. Med.* **186**, 325–330 (1997).
51. Kishimoto, H. & Sprent, J. Strong TCR ligation without costimulation causes rapid onset of Fas-dependent apoptosis of naive murine CD4$^+$T cells. *J. Immunol.* **163**, 1817–1826 (1999).
52. Kabsch, W. Xds. *Acta Crystallogr. D Biol. Crystallogr.* **66**, 125–132 (2010).
53. Vagin, A. & Teplyakov, A. Molecular replacement with MOLREP. *Acta Crystallogr. D Biol. Crystallogr.* **66**, 22–25 (2010).
54. Emsley, P., Lohkamp, B., Scott, W. G. & Cowtan, K. Features and development of Coot. *Acta Crystallogr. D Biol. Crystallogr.* **66**, 486–501 (2010).
55. Davis, I. W. et al. MolProbity: all-atom contacts and structure validation for proteins and nucleic acids. *Nucleic Acids Res.* **35**, W375–W383 (2007).
56. Krissinel, E. & Henrick, K. Secondary-structure matching (SSM), a new tool for fast protein structure alignment in three dimensions. *Acta Crystallogr. D Biol. Crystallogr.* **60**, 2256–2268 (2004).
57. Pascall, J. C. et al. The immune system GTPase GIMAP6 interacts with the Atg8 homologue GABARAPL2 and is recruited to autophagosomes. *PLoS ONE* **8**, e77782 (2013).
58. Yao, Y. et al. Mucus sialylation determines intestinal host-commensal homeostasis. *Cell* **185**, 1172–1188 (2022).
59. Cook, S. A. et al. HEM1 deficiency disrupts mTORC2 and F-actin control in inherited immunodysregulatory disease. *Science* **369**, 202–207 (2020).
60. Lucas, C. L. et al. Dominant-activating germline mutations in the gene encoding the PI(3)K catalytic subunit p110δ result in T cell senescence and human immunodeficiency. *Nat. Immunol.* **15**, 88–97 (2014).
61. Lo, B. et al. Autoimmune disease. Patients with LRBA deficiency show CTLA4 loss and immune dysregulation responsive to abatacept therapy. *Science* **349**, 436–440 (2015).

Acknowledgements

The authors thank the physicians, patients and families participating in this study; University of Washington Center for Mendelian

Genomics for Geno2MP; L. Folio for preparation of clinical data; the late Professor I. Barlan for helping initiate the study; NIAID Biological Imaging Section; C. Schwartz (Electron Microscopy Unit, Research Technologies Section, Rocky Mountain Laboratories, National Institute of Allergy and Infectious Diseases) for EM analysis; R. Kissinger (Visual Medical Arts, Research Technologies Branch, Rocky Mountain Laboratories, NIAID) for illustrations; D. E. Anderson (Advanced Mass Spectrometry Core, National Institute of Diabetes and Digestive and Kidney Diseases); F. Meylan (National Institute of Arthritis and Musculoskeletal and Skin Diseases); and H. Bulut for help in the thermal unfolding assays. We thank R. Perlmutter and J. McElwee for advice and support and acknowledge generous support from Merck. We thank NIAID Central Sequencing Initiative for patient referral and advice. Finally, we thank R. N. Germain, L. M. Staudt and A. L. Snow for critically reading the manuscript.

This work was supported by the Division of Intramural Research, NIAID, NIH and Merck and Co.; German Research Foundation SFB958, project A12 (O.D.); NIH-NIDDK, K08 DK113109 and R01 DK131033 (S.V.); Biotechnology and Biological Sciences Research Council BBS/E/B/000C0407 and BBS/E/B/000C0427 (G.B. and J.P.); The Scientific and Technological Research Council of Turkey 318S202 (S.B.); Recurrent institutional funding from INSERM, CEA, Ligue Nationale contre le Cancer, University Grenoble Alpes (C.C. and O.F.); and TUBITAK-1003 Project, project ID 315S125 (A.I., S.H. and F.D.). Figures 2g, 4a and 6e and Extended Data Fig. 6b were created with BioRender.com.

Author contributions

Conceptualization was the responsibility of A.Y.P., M.L.-G., M.L., J.Q.G., X.X., B.C., H.C.S. and M.J.L. Data curation was the responsibility of A.Y.P., M.L.-G., M.L., J.Q.G., X.X., B.S., L.Z., A.B., H.H., B.C., J.C., Y.Y., S.K., J.M.C., A.R.M., P.J., J.C.R., Y.H.C., A.G., A.F., S.G., J.A., J.E.-H., E.B., H.O., H.M., C.C., O.F. and D.S. Formal analysis was carried out by A.Y.P., M.L.-G., M.L., J.Q.G., X.X., B.S., L.Z., A.B., B.C., Y.Z., A.R.M., S.A.C., Y.H.C., S.D.C., J.A., J.E.-H., C.C., O.F. and D.S. Funding acquisition was the responsibility of G.W.B., J.P., F.D., C.C., O.F., O.D., S.H., A.I., S.V., S.B., H.C.S. and M.J.L. Investigation was conducted by A.Y.P., M.L.-G., M.L., J.Q.G., X.X., B.S., L.Z., A.B., B.C., J.E.-H., C.C., O.F., D.S., H.C.S. and M.J.L. Methodology was the responsibility of A.Y.P., M.L.-G., M.L., J.Q.G., X.X., B.S., L.Z., A.B., B.C., Y.Z., H.M., A.M.P., L.X. and D.S. Resources were the responsibility of H.F.M., C.T., G.W.B., J.P., E.K.-A., A.K., İ.T., S.E., R.J.H., D.A., S.T., A.K., Z.K., E.U., T.K., F.D., E.K., T.P.A., C.A., G.E.Ş., A.Ü.A., G.U., V.K.R., S.S., B.D., K.B., D.C., S.H., A.I., S.V., S.B. and A.O.; Supervision was carried out by C.M.B., M.M.D., R.P.L., E.L.P., O.D., H.C.S. and M.J.L. Writing of the original draft was carried out by A.Y.P., M.L.-G. and M.J.L. Review and editing was carried out by A.Y.P., M.L.-G., M.L. J.Q.G., B.S., L.Z., A.B., S.A.C., J.R.E.B., O.D., D.S., H.C.S. and M.J.L.

Competing interests

The authors declare no competing interests.

Additional information

Extended data is available for this paper at https://doi.org/10.1038/s41590-023-01691-y.

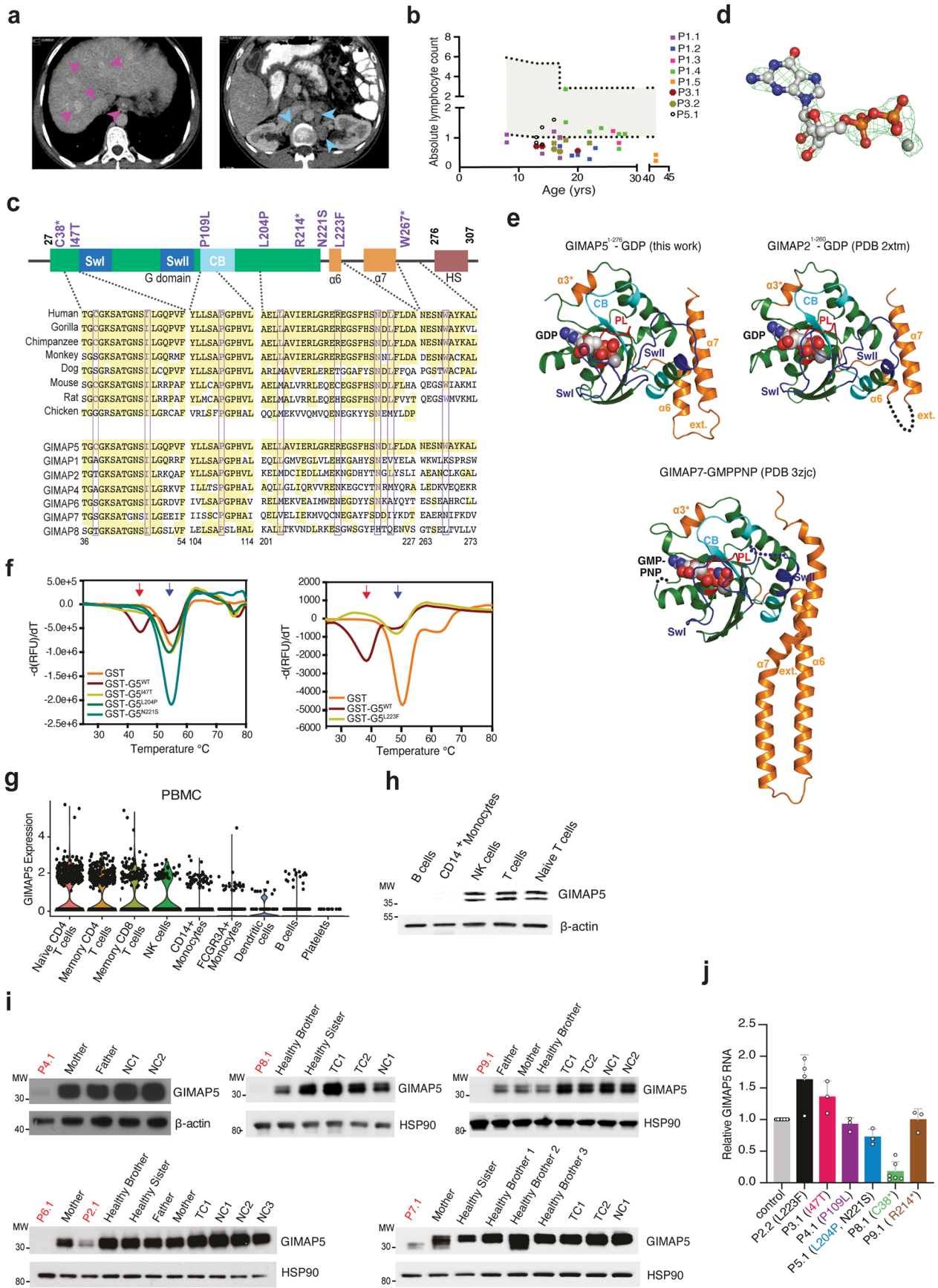
Supplementary information The online version contains supplementary material available at https://doi.org/10.1038/s41590-023-01691-y.

Correspondence and requests for materials should be addressed to Michael J. Lenardo.

Peer review information *Nature Immunology* thanks Takeshi Nitta, Claudio Mauro, and the other, anonymous, reviewer(s) for their contribution to the peer review of this work. Primary Handling Editor: L. A. Dempsey, in collaboration with the *Nature Immunology* team.

Reprints and permissions information is available at www.nature.com/reprints.

https://doi.org/10.1038/s41590-023-01691-y

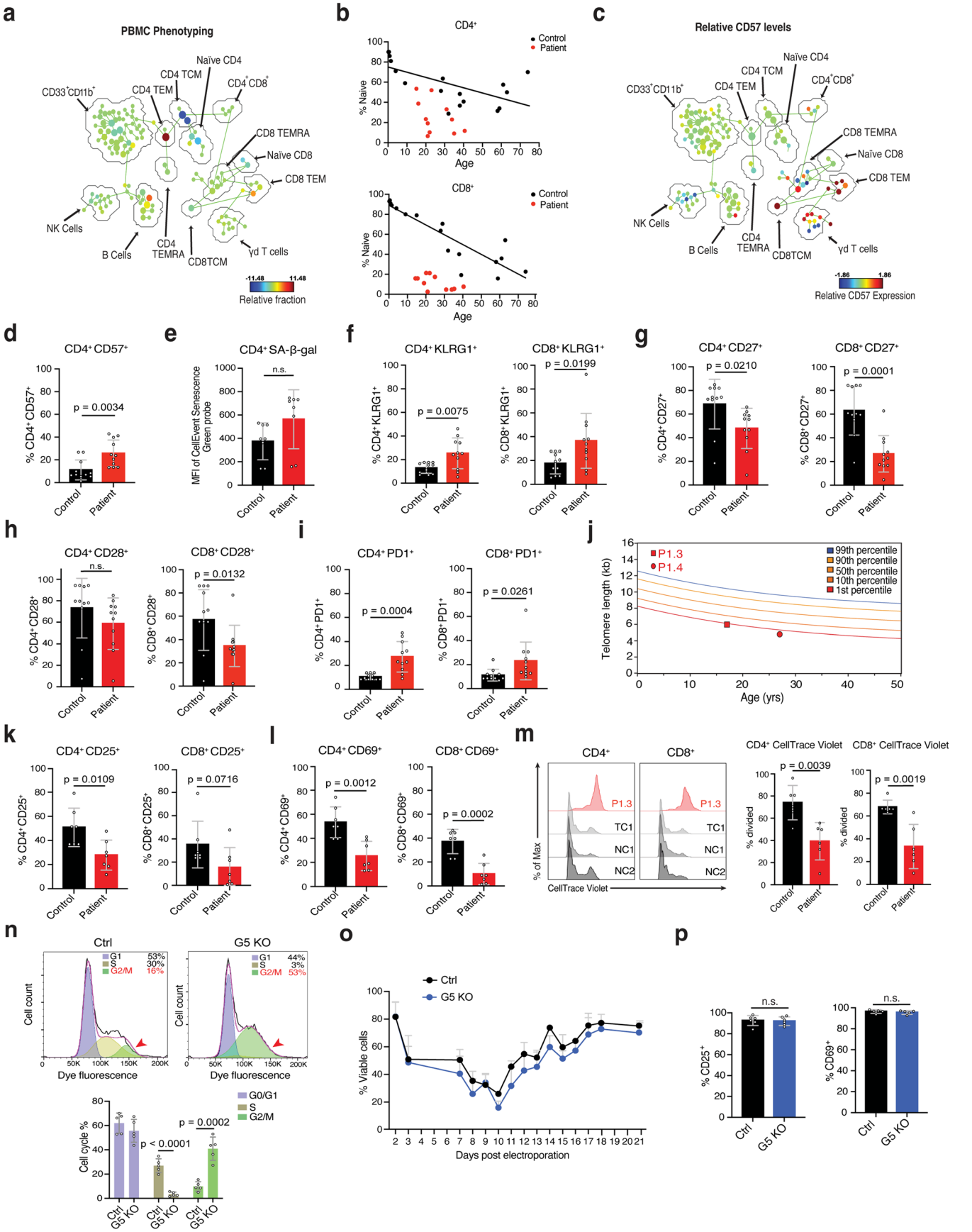


Extended Data Fig. 1 | See next page for caption.

https://doi.org/10.1038/s41590-023-01691-y

Extended Data Fig. 1 | GIMAP5 mutations cause protein destabilization in patients' T cells. a, Computerized tomography scan of P7.1 showing liver nodules (left, magenta arrowheads) and esophageal varices (right, cyan arrowheads) suggesting liver failure. **b**, Absolute lymphocyte counts versus patient age (years, yrs), shaded area representing 95% confidence interval for normal range. **c**, Patient amino acid substitutions on GIMAP5 protein schematic (top). GTPase (G) domain: green; switch I (SwI) and switch II (SwII): blue; conserved box (CB): cyan; alpha helices (α) 6 and 7: orange; hydrophobic segment: maroon. Amino acid alignment in GIMAP5 orthologues and 7 human paralogues (bottom). Mutations marked in purple and boxed. **d**, Omit F_o-F_c density map for GDP and the Mg^{2+} ion bound to GIMAP5$^{1-276}$, contoured at 3σ (green). The refined GDP•Mg^{2+} molecules shown in ball-and-stick. **e**, Comparison of GIMAP5$^{1-276}$-GDP (left), GIMAP2$^{1-260}$-GDP (middle, PDB code 2xto), and GIMAP7 L100Q-GMPPNP (right, PDB code 3zjc). G domains: green; switch I (SwI) and switch II (SwII): purple; P-loops (PL): red; conserved box (CB): cyan; nucleotides: space-filling spheres; secondary structure elements differing from the core G domain of H-Ras, helices α3* and the C-terminal helices α6 and α7 (C-terminal extension, ext.): orange; unstructured loops; dotted lines. Root mean square deviation of aligned Cα atoms: 1.4 Å (GIMAP5 vs. GIMAP2) and 2.0 Å (GIMAP5 vs. GIMAP7). **f**, Thermal denaturation profiles. GST- WT GIMAP5$^{1-276}$ displayed two temperature transitions - GIMAP5$^{1-276}$ unfolding (red arrow) and GST unfolding (blue arrow). GST-GIMAP5$^{1-276}$ variants (left: I47T, L204P and N221S; right: L223F) showed a single transition, representing GST unfolding, with no WT GIMAP5$^{1-276}$ transition. Left and right experiments were conducted in separate laboratories. **g**, Single-cell GIMAP5 RNA expression in human peripheral blood mononuclear cells (PBMCs). **h**, Immunoblots of GIMAP5 in primary human CD19$^+$ B cells, CD14$^+$ monocytes, CD56$^+$ NK cells, and T cells with β-actin loading control (n = 3). **i**, Immunoblots of GIMAP5 from patients (P), family, normal control (NC) or shipping control (TC) T cell lysates with a b-actin or an HSP90 loading control (n = 3). **j**, GIMAP5 RNA expression by RT-qPCR in patients (n = 6) and controls (n = 6) normalized to 18S. Samples were examined over at least 3 independent experiments (mean ± s.d.).

https://doi.org/10.1038/s41590-023-01691-y

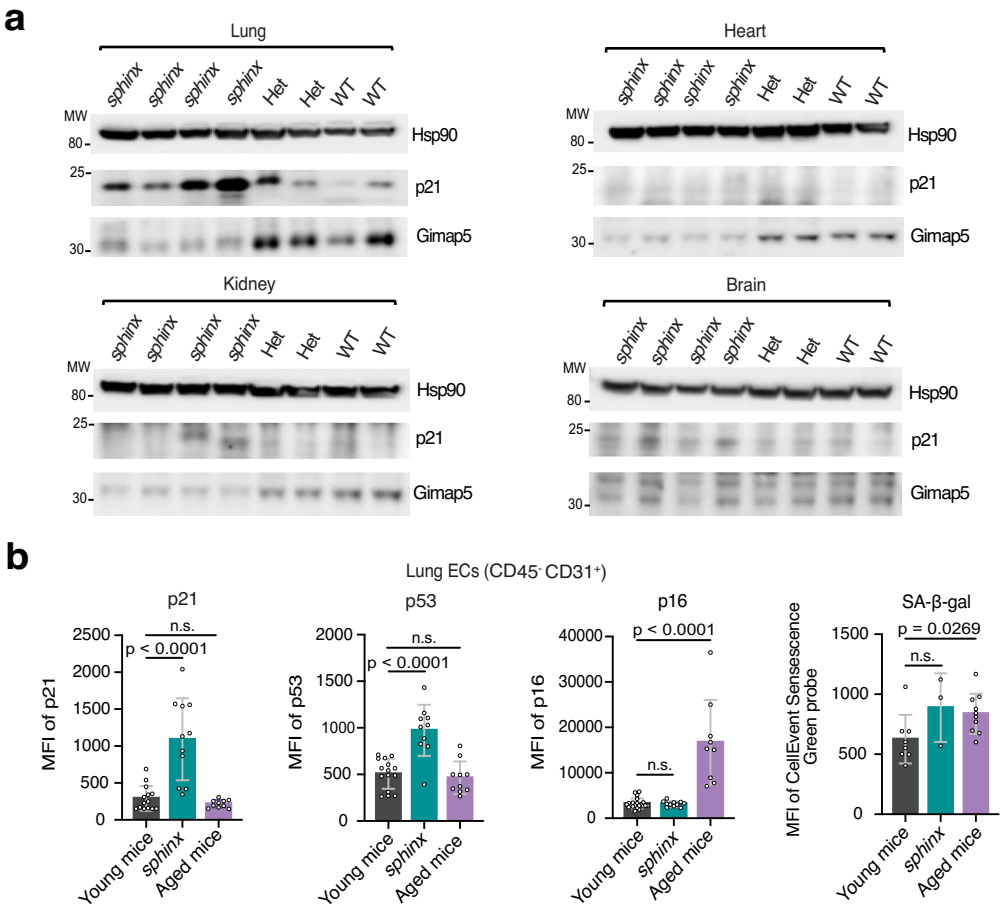


Extended Data Fig. 2 | See next page for caption.

https://doi.org/10.1038/s41590-023-01691-y

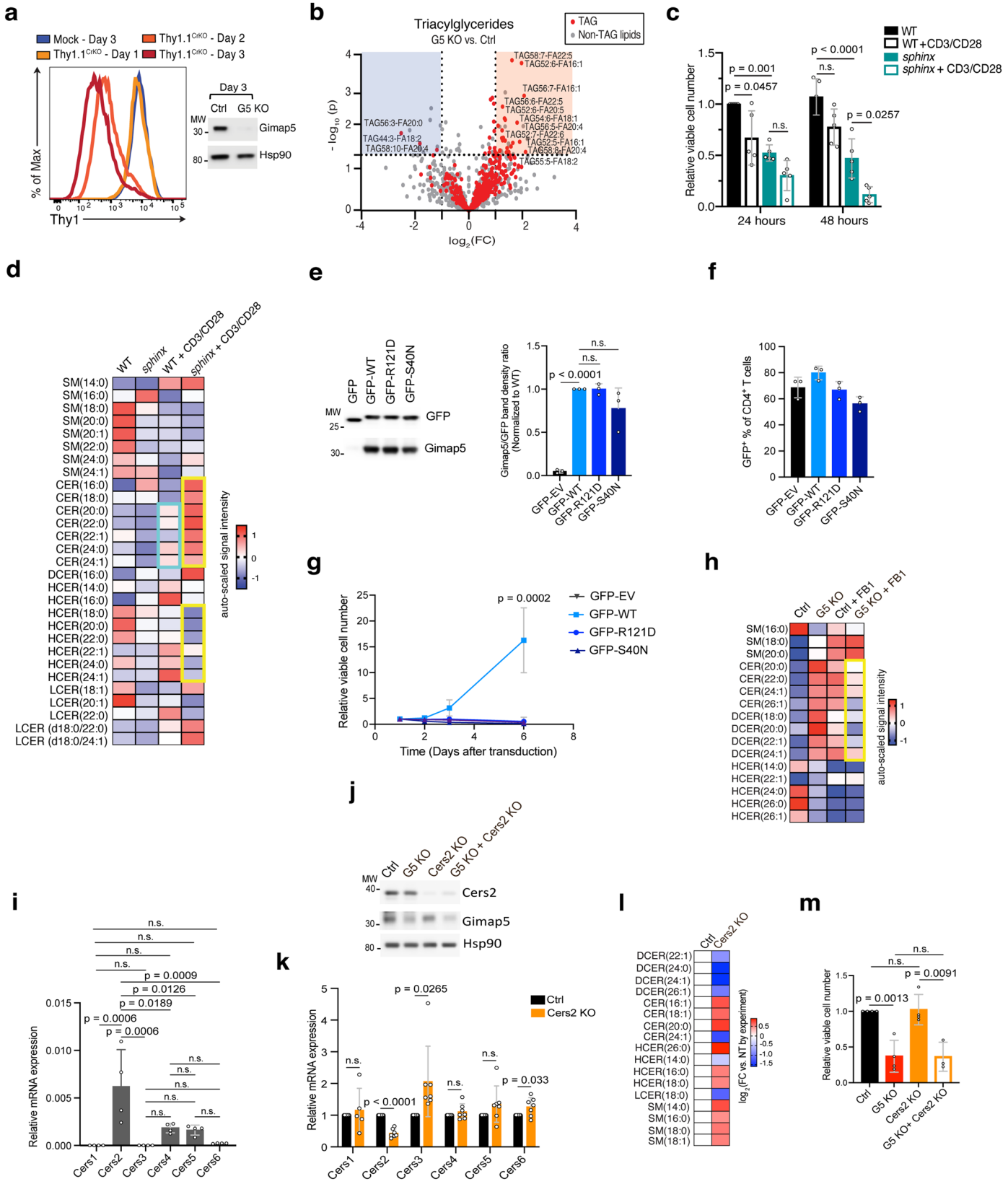
Extended Data Fig. 2 | GIMAP5 deficiency induces senescence in human T cells. a, CyTOF mass cytometry from patient (P1.3, P1.4) or control (n = 8) PBMCs. NK = natural killer; TEM = T effector memory; TEMRA = Terminally differentiated effector memory; TCM = T central memory. **b**, Percent of patient (red, n = 11) and control (black, $CD4^+$: n = 16, $CD8^+$: n = 17) naive T cells against age in years. Simple linear regression of control data (black line). **c**, Phenotyping CyTOF, depicting relative CD57 levels as in (a). **d**, Percent of $CD4^+CD57^+$ T cells. Controls (n = 42), Patients (n = 11). **e**, MFI of SA-β-gal activity in $CD4^+$ T cells. Controls (n= 16), patients (n = 8). **f-i**, Percent of $KLRG1^+$ (f, controls: n = 24, patients: n = 11), $CD27^+$ (g, controls: n = 30, patients: n = 11), $CD28^+$ (h, controls: n = 28, patients: n = 11), and $PD1^+$ (i, controls: n = 32, patients: n = 11) in T cells. **j**, Telomere length in kilobases (kb) against age in years (yrs) for P1.3 and P1.4 lymphocytes. Colored lines indicate percentile isobars. **k, l**, Percent of CD25 (k) or CD69 (l) on T cells 24 hours post-activation. Controls (n = 15), patients (n = 7). **m**, Proliferation via CellTrace Violet dilution in T cells (3 days post-activation, left two panels). Normal controls (NC), Shipping controls (TC). % divide quantified (right two panels). Controls (n = 15), patients (n = 6). **n**, DNA content in Ctrl or G5 KO human T cells on day 16 post-electroporation (upper). Percent of Ctrl and G5 KO T cells in the indicated phases (bottom). Red arrowhead indicates G2/M population (n = 5). **o**, Percent of viable G5 KO or Ctrl human T cells over time post-electroporation (n = 6 per group). **p**, Percent of CD25 (left) and CD69 (right) on G5 KO or Ctrl human naïve T cells 24 hours after CD3/CD28 Dynabeads activation, 5 days post-electroporation (n = 5 per group). All data are mean ± s.d. and were analyzed by two-tailed, unpaired Student's t-test (b,f). n.s. = not significant. $p < 0.0001$: in **n**, $p = 2.11 \times 10^{-5}$.

https://doi.org/10.1038/s41590-023-01691-y



Extended Data Fig. 3 | Gimap5 deficiency in mice induces a partial senescence phenotype in lung endothelial cells (ECs). a, Immunoblots of heart, kidney, and brain tissue lysates from *sphinx* (*Gimap5*$^{sph/sph}$), Het (*Gimap5*$^{+/sph}$) and WT (wild-type) mice for Gimap5, p21 and Hsp90. Representative immunoblots from two independent experiments are shown. Littermate controls (n = 8), *sphinx* (n = 7). Note that bands detected in Gimap5 brain tissue immunoblot are unaffected by *sphinx* mutation, implying background signals. **b**, MFI of p21, p53, p16 and SA-β-gal activity in CD45$^-$CD31$^+$ lung ECs from young mice (littermate controls), *sphinx*, and aged mice. CD45$^-$CD31$^+$ p21: young mice (n = 14), *sphinx* (n = 11), aged mice (n = 10); CD45$^-$CD31$^+$ p53: young mice (n = 15), *sphinx* (n = 10), aged mice (n = 10); CD45$^-$CD31$^+$ p16: young mice (n = 21), *sphinx* (n = 11), aged mice (n = 10); CD45$^-$CD31$^+$ SA-β-gal: young mice (n = 8), *sphinx* (n = 3), aged mice (n = 10). 7- to 12-week-old (young, *sphinx*) or 16 to 19-month-old (aged) male and female mice were used in each experiment. All data are mean ± s.d. and were analyzed by two-tailed, unpaired Student's t-test (b). n.s. = not significant. p < 0.0001: in **b** (left to right), $p = 3.49 \times 10^{-5}$, $p = 1.89 \times 10^{-5}$, $p = 4.23 \times 10^{-6}$.

https://doi.org/10.1038/s41590-023-01691-y

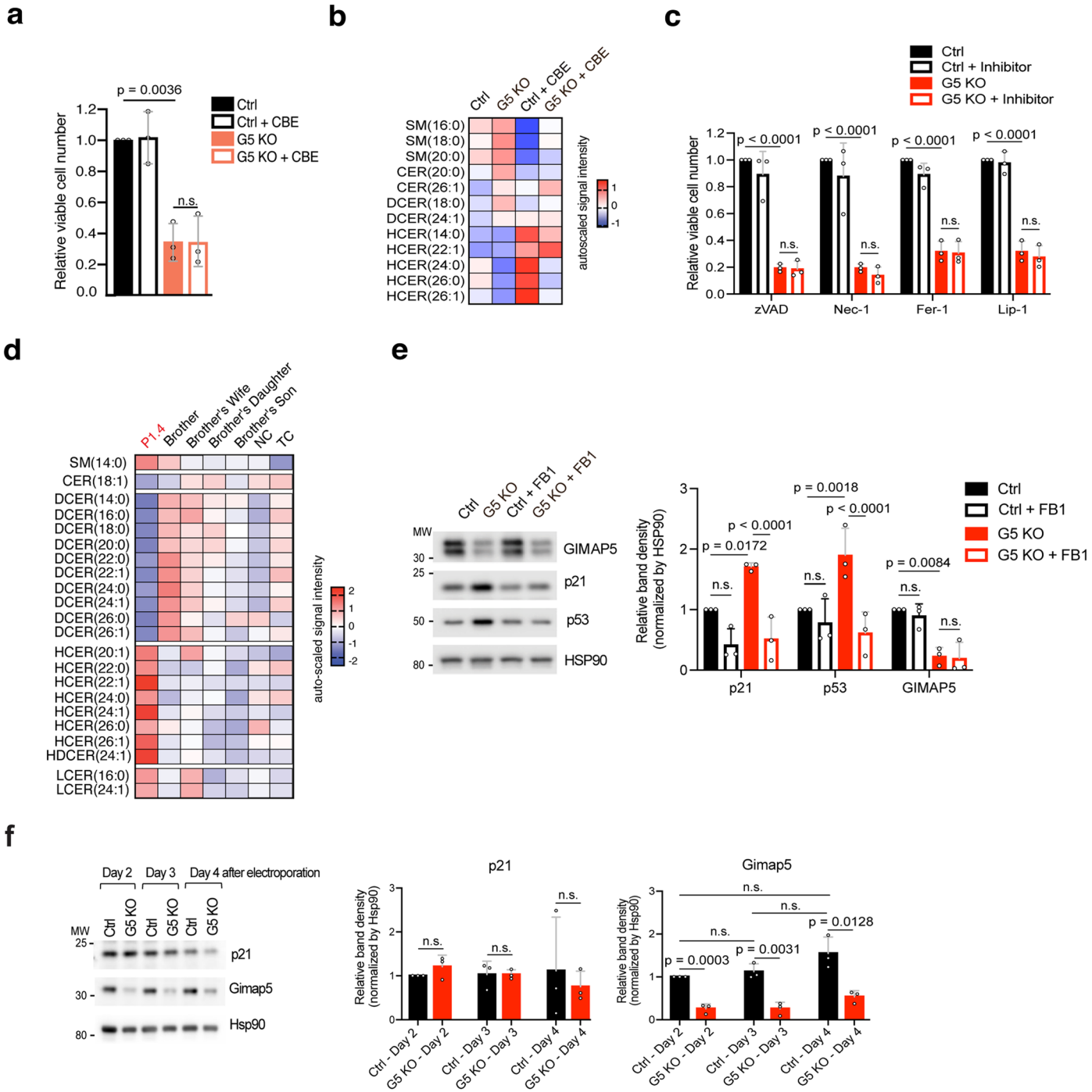


Extended Data Fig. 4 | See next page for caption.

https://doi.org/10.1038/s41590-023-01691-y

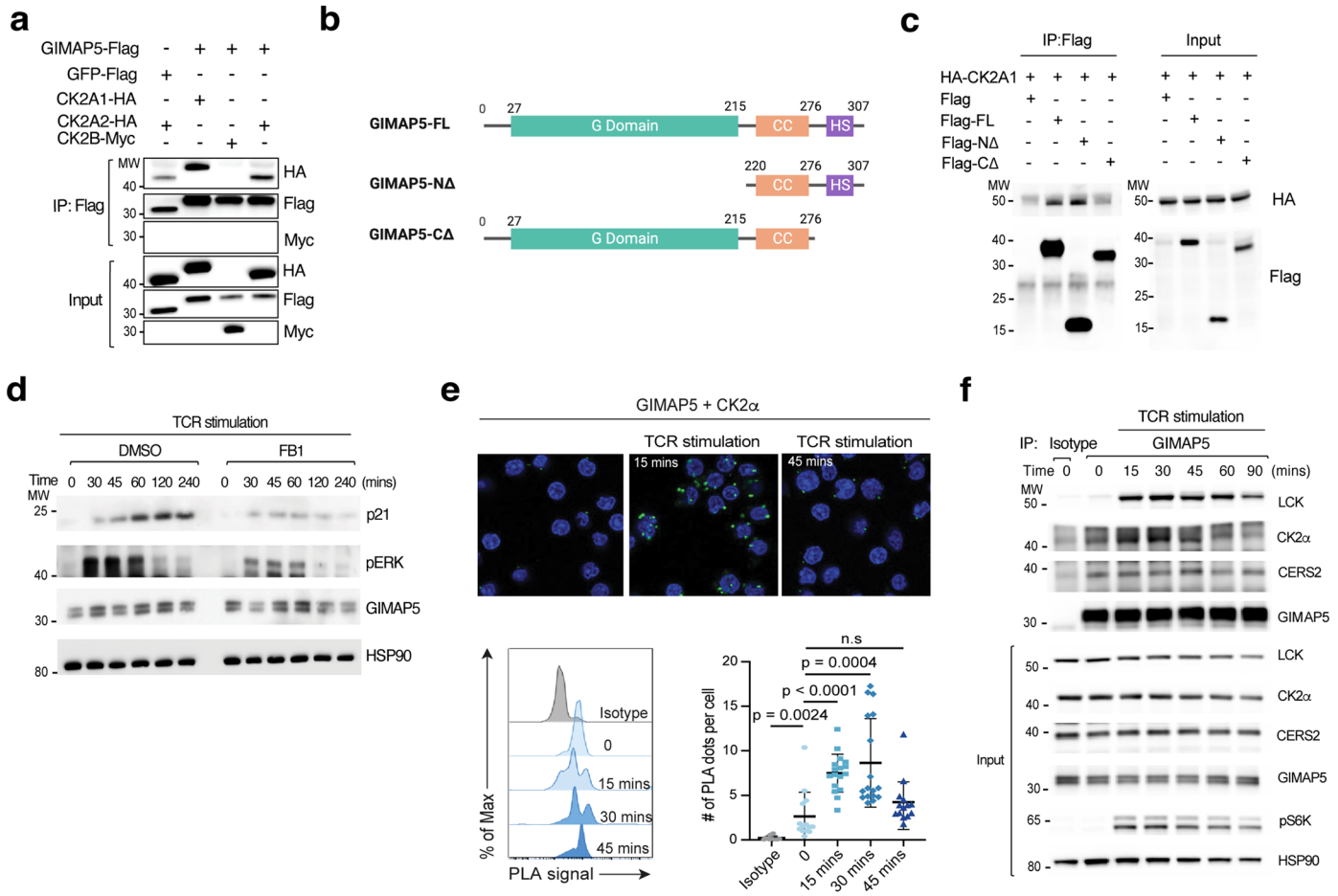
Extended Data Fig. 4 | GIMAP5 controls the levels of CER and TAG. a, Thy1.1 levels in murine T cells post-electroporation (left). Immunoblot of indicated proteins from left (day 3 post-electroporation, right)(n = 5). **b**, Volcano plot of lipids in G5 KO murine T cells vs. Ctrl, day 3 post-electroporation. Triacylglyceride (TAG) species, red (n = 5). **c**, Viable $CD4^+$ T cell numbers from WT or *Gimap5*$^{sph/sph}$ (*sphinx*) mice with IL-7 (unstimulated) or stimulated with anti-CD3/CD28 antibodies, relative to unstimulated WT (n = 4)**. d**, SPL heat map of 24-hour samples from (**c**), key changes in cyan or yellow boxes (FDR ≤ 0.05) (n = 5). **e**, Immunoblots of NIH-3T3 cells following indicated transductions (left)(n = 3 per group). **f**, Percent of GFP^+CD4^+ T cells, day 2 post-transduction in *Gimap5*$^{sph/sph}$ $CD4^+$ T cells (n = 3 per group). **g**, Relative viable cell numbers in GFP^+CD4^+ T cells from (f) over time (n = 3 per group). **h**, SPL heat map of Ctrl and G5 KO murine T cells from Fig.4f, day 3 post-electroporation. Only significant SPLs from Fig. 4e are displayed (p ≤ 0.05) (n = 5). **i**, Murine T cell Cers relative mRNA expression (RT-qPCR, normalized to Gapdh)(n = 4 per group). **j**, Immunoblots of indicated proteins in indicated murine KO T cells, day 3 post-electroporation (n = 3). **k**, Relative mRNA expression of Cers1-6, in Ctrl and Cers2 KO murine T cells, day 3 post-electroporation (RT-qPCR, normalized to Ctrl KO)(Cers1: n = 5 per group, Cers2-6: n = 7 per group). **l**, SPL heat map of Ctrl and Cers2 KO murine T cells, p values < 0.1, all samples normalized to Ctrl (n = 3). **m**, Relative viable cell numbers of murine T cell blasts from (j) (Ctrl, G5 KO, Cers2 KO: n = 4, G5 KO + Cers2 KO: n = 3). All data are mean ± s.d. and were analyzed by two-tailed, unpaired Student's t-test (b,h,g,k,l,m) or by two-way ANOVA with Bonferroni post-test (c,e,i). n.s. = not significant. p < 0.0001: in **c**, $p = 7.33 \times 10^{-6}$, in **e** (left to right), $p = 3.42 \times 10^{-5}$, $p = 3.39 \times 10^{-5}$, in **k**, $p = 1.19 \times 10^{-7}$.

https://doi.org/10.1038/s41590-023-01691-y



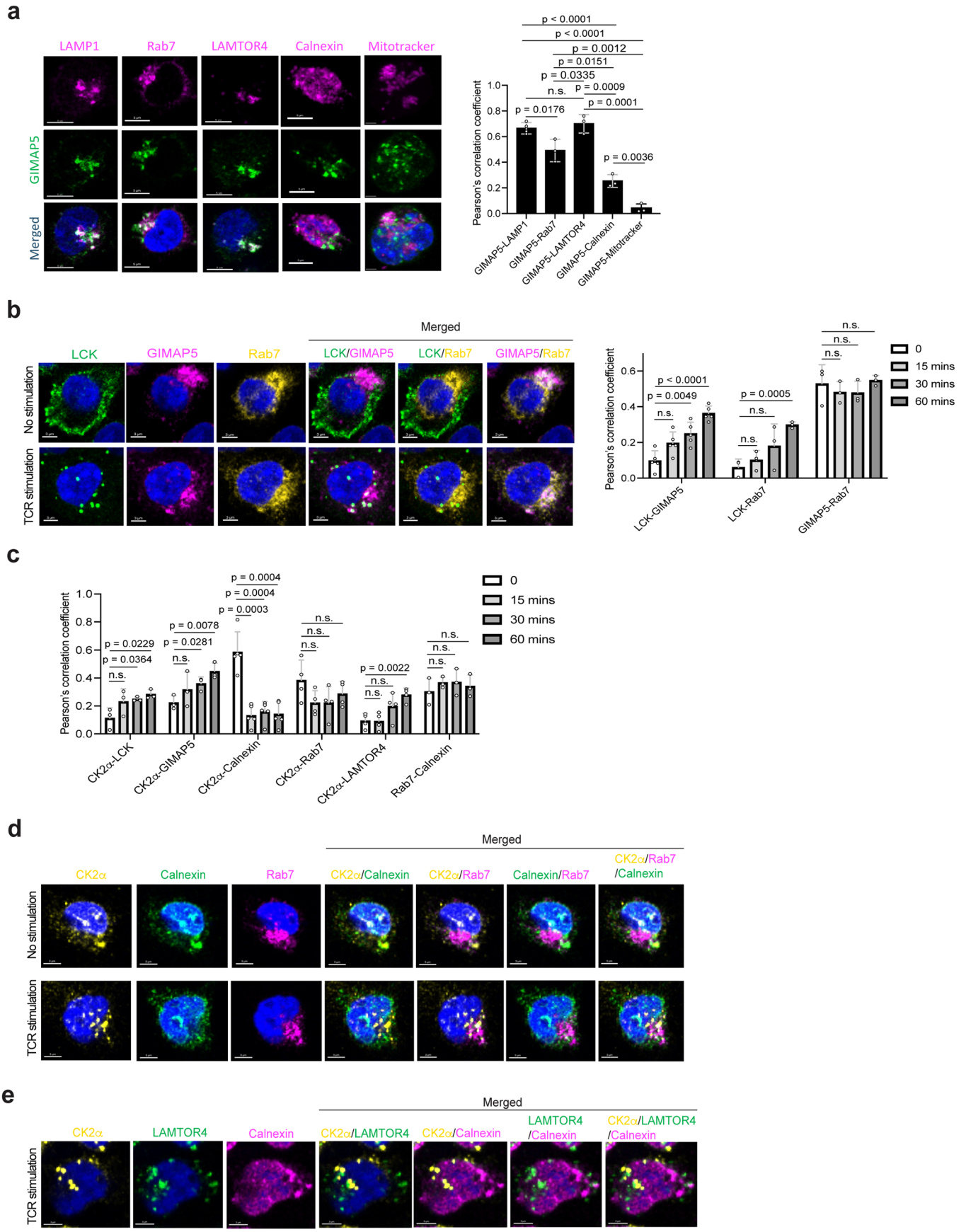
Extended Data Fig. 5 | GIMAP5 controls the levels of CER, thereby regulating cell survival or cell senescence. a, Relative viable cell number of Ctrl and G5 KO murine T cell blasts treated with 200 µM conduritol-β-epoxide (CBE), starting on day 1 post-electroporation, measured on day 3 post-electroporation (n = 3 per group). **b**, Heat map of SPLs detected in (a) using the z scale indicated. Only SPLs found to be significantly affected in Fig. 4e are displayed ($p \leq 0.05$) (n = 3). **c**, Relative viable cell number of Ctrl and G5 KO murine T cell blasts treated with zVAD (20 µM), necrostatin-1 (Nec-1, 20 µM), ferrostatin-1 (Fer-1, 3 µM) or liproxstatin-1 (Lip-1, 3 µM) on day 1 and quantified on day 3 post-electroporation (n = 3 per group). **d**, Heat map of SPLs detected in P1.4, healthy family members, normal controls (NC) or shipping controls (TC). Hits on the heatmaps are >1 standard deviation from the mean (>1 z-score) (n = 3). **e**, Immunoblots of Ctrl or G5 KO human T cell lysates treated with FB1 (10 µM, 24 hr) for proteins shown (left). WCLs were collected as in Fig. 2i. Quantified left panel bands with ImageJ (right). Bands normalized to HSP90, and relative intensities presented as Ctrl vs. each sample (n = 3 per group). **f**, Immunoblot analysis of p21 and Gimap5, with Hsp90 loading control, in Ctrl or G5 KO murine T cells on day 2, 3, and 4 post-electroporation (left). Quantification of p21 and Gimap5 band intensities from left panel using ImageJ (center and right). Bands of interest, normalized to Hsp90, show relative intensities compared to Ctrl (day 2 post-electroporation) for each sample (n = 3 per group). All data are mean ± s.d. and were analyzed by two-tailed, unpaired Student's t-test (a,b,f) or by two-way ANOVA with Bonferroni post-test (c,e). n.s. = not significant. $p < 0.0001$: in **c** (left to right), $p = 4.35 \times 10^{-11}$, $p = 4.35 \times 10^{-11}$, $p = 2.25 \times 10^{-9}$, $p = 2.25 \times 10^{-9}$, in **e** (left to right), $p = 5.46 \times 10^{-5}$, $p = 1.89 \times 10^{-5}$.

https://doi.org/10.1038/s41590-023-01691-y



Extended Data Fig. 6 | GIMAP5 interacts with CK2 and LCK. a, HEK293T cells were transfected with tagged plasmids expressing GFP-Flag, GIMAP5-Flag, CK2A1-HA, CK2A2-HA or CK2B-Myc, as indicated by a plus sign. Cell lysates were prepared 24 hours post transfection (Input), immunoprecipitated (IP) for Flag tag, and immunoblotted with the indicated antibodies (n = 3). **b**, Schematic diagram illustrating GIMAP5 full-length (FL), GIMAP5 N-terminal 219-amino-acid (G domain) truncated mutant (GIMAP5 NΔ), and GIMAP5 C-terminal 30-amino-acid (hydrophobic domain) truncated mutant (GIMAP5 CΔ). **c**, HEK293T cells were transiently transfected with Flag, Flag-GIMAP5 FL, Flag-GIMAP5 NΔ, Flag-GIMAP5 CΔ, or HA-CK2A1, as indicated by a plus sign. Cell lysates were prepared 24 hours post transfection (Input), immunoprecipitated (IP) for Flag tag, and immunoblotted with Flag and HA antibodies (n = 3). **d**, Immunoblots of p21, pERK (phospho-ERK1/2), and GIMAP5 with an HSP90 loading control. Cell lysates were collected from human T cell blasts with or without CERS inhibitor, FB1 (20 μM) pretreatment (1 hr) followed by TCR stimulation for the indicated times in minutes (mins) (n = 3). Note that the variable GIMAP5 expression levels were not detected in other repeats. **e**, Confocal microscopy of GIMAP5 + CK2α (top) in PLA after TCR stimulation as in Fig. 5b. PLA signals were quantified by flow cytometry (bottom left) and by the number of PLA dots per cell (bottom right) (3 biological replicates; Isotype: n = 381 from 14 images; 0: n = 390 from 14 images; 15 mins: n = 395 from 17 images; 30 mins: n = 487 from 17 images; 45 mins: n = 491 from 14 images). **f**, Immunoprecipitation (IP) with anti-GIMAP5 or isotype control in human T cell blasts after TCR stimulation for multiple timepoints measured in minutes (mins) (n = 6). Two-tailed, unpaired Student's t-test (**f**; mean ± s.d.). n.s. = not significant. $p < 0.0001$: in **e**, $p = 4.75 \times 10^{-6}$.

https://doi.org/10.1038/s41590-023-01691-y

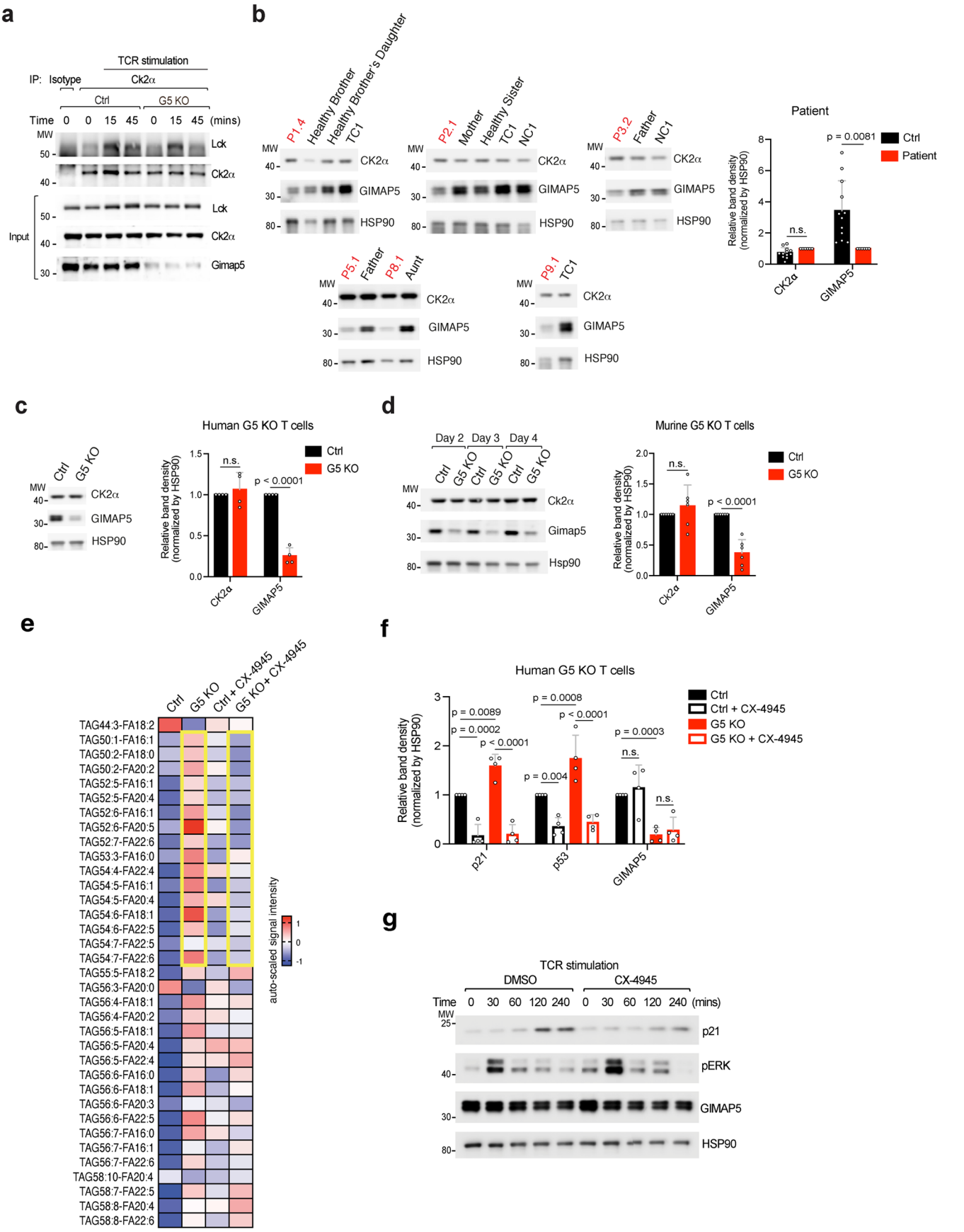


Extended Data Fig. 7 | See next page for caption.

https://doi.org/10.1038/s41590-023-01691-y

Extended Data Fig. 7 | GIMAP5 colocalizes with CK2α and LCK after TCR stimulation at the late endosome/lysosome. a, Immunofluorescence staining with LAMP1, Rab7, LAMTOR4, Calnexin or MitoTracker (magenta) and GIMAP5 (green) in human T cell blasts (left). Colocalization of indicated markers by Pearson's correlation coefficient (PCC) (right). n (left to right): 485, 907, 566, 507, 412. **b**, Immunofluorescence staining with anti-LCK (green), GIMAP5 (magenta), and Rab7 (yellow) in human T cell blasts before and after TCR stimulation (60 mins) (left). Colocalization of indicated markers before and after TCR stimulation by PCC (right). n (left to right): 2664, 3071, 2751, 2388, 1419, 1570, 1411, 1181, 1419, 1570, 1411, 1181. **c**, Colocalization of CK2α with LCK, GIMAP5, Calnexin, Rab7, and LAMTOR4 and Rab7 with Calnexin before and after TCR stimulation by PCC. n (left to right): 2226, 2382, 2191, 2042, 1426, 1716, 1521, 1377, 2502, 2387, 2484, 2139, 1865, 1599, 2118, 1625, 1653, 2000, 2091, 1501, 1630, 1473, 1219, 1361. **d**, Immunofluorescence staining with anti-CK2α (yellow), Calnexin (green), and Rab7 (magenta) in human T cell blasts before and after TCR stimulation (60 mins). **e**, Immunofluorescence staining with anti-CK2α (yellow), LAMTOR4 (green), and Calnexin (magenta) in human T cell blasts after TCR stimulation (60 mins). Representative of at least three biological replicates (a,b,d,e). All data are mean ± s.d. and were analyzed by two-tailed, unpaired Student's t-test (a,c) or by two-way ANOVA with Bonferroni post-test (b). n.s. = not significant. $p < 0.0001$: in **a** (left to right), $p = 8.41 \times 10^{-5}$, $p = 5.62 \times 10^{-6}$, in **b**, $p = 1.68 \times 10^{-6}$.

https://doi.org/10.1038/s41590-023-01691-y

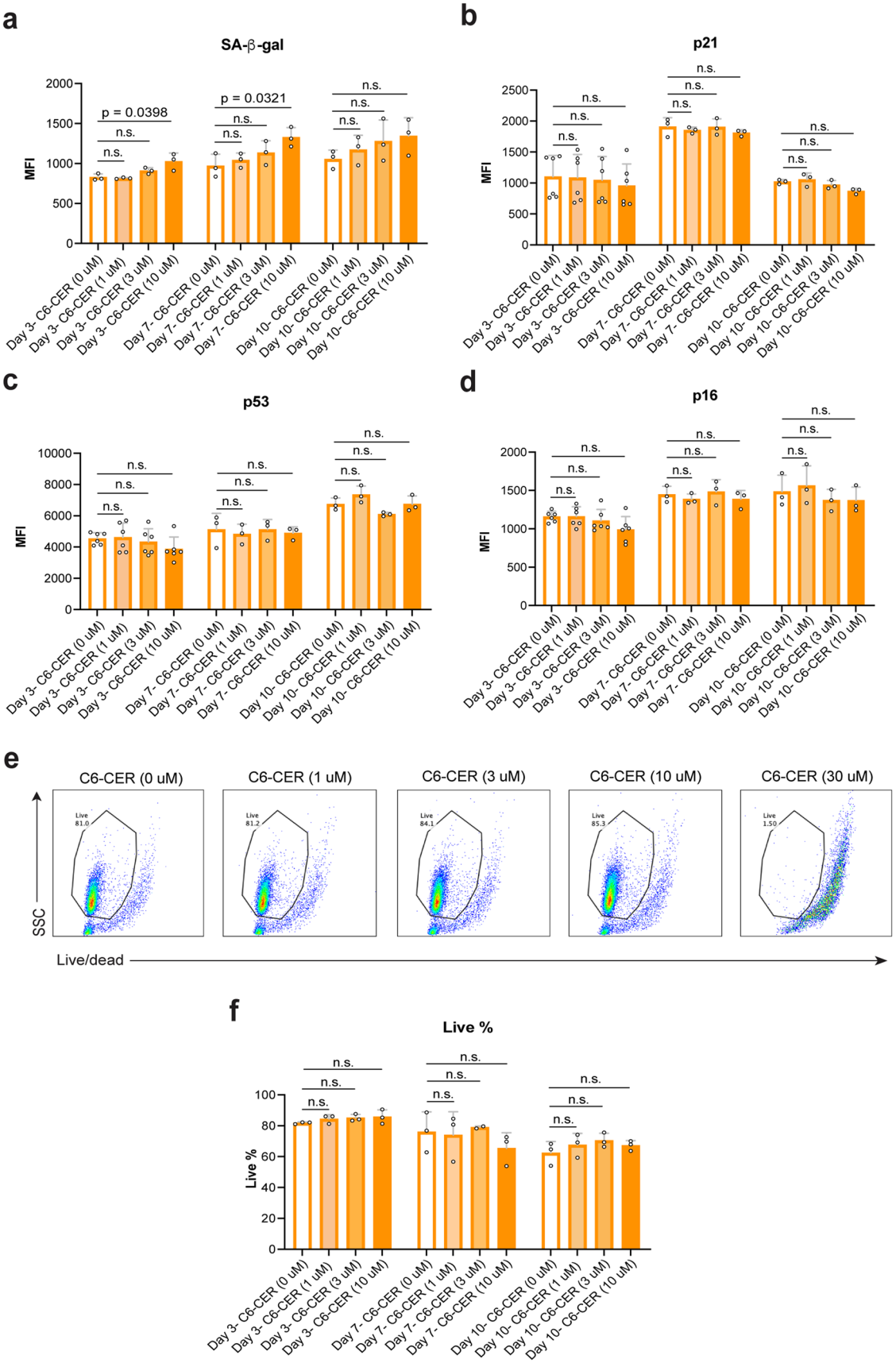


Extended Data Fig. 8 | See next page for caption.

https://doi.org/10.1038/s41590-023-01691-y

Extended Data Fig. 8 | GIMAP5 controls the levels of CER and TAG through its association with CK2 without affecting the level of CK2. a, Immunoprecipitation with anti-Ck2α or isotype control in control or G5 KO murine T cell blasts after TCR stimulation (n = 3). **b**, Immunoblots of T cell lysates from patients, family members, and healthy donors (NC = normal control, TC = shipping control) for the indicated proteins (left). Whole cell lysates (WCL) were collected between 7 to 15 days post-activation. Quantified left panels with ImageJ (right, Ctrl: n = 12; patient: n = 6). Bands normalized to HSP90. **c**, Immunoblots of Ctrl or G5 KO human T cells for the indicated proteins (left). WCLs from human T cell blasts were collected 16 days post-activation. Quantified left bands with ImageJ (right). Bands normalized to HSP90 (n = 4 per group). **d**, Immunoblots of Ctrl or G5 KO murine T cells for the indicated proteins (left). WCLs from murine T cell blasts were collected on days 2, 3, and 4 post-electroporation. Quantified bands from 3 days post-electroporation samples using ImageJ (right). Bands normalized to Hsp90 (n = 6 per group). **e**, Signal intensity of TAG species in Ctrl and G5 KO murine T cell blasts, 3 days post-electroporation, treated with 2.5 μM CK2 inhibitor CX-4945 on day 1 post-electroporation. Only significant TAGs from Extended Data Fig. 4b are shown ($p \leq 0.05$). Key changes in yellow boxes. Signal levels reflect the total sum normalized and auto-scaled (n = 5). **f**, Quantified Fig. 5j bands with ImageJ, normalized to HSP90 bands, and presented relative intensities compared to Ctrl (untreated) for each sample (n = 4 per group). **g**, Immunoblots of cell lysates for proteins shown. WCLs were collected after CX-4945 or dimethylsulfoxide (DMSO) vehicle pretreatment (1 hr) followed by TCR stimulation. (n = 4). All data are mean ± s.d. and were analyzed by two-tailed, unpaired Student's t-test (b-e) or by two-way ANOVA with Bonferroni post-test (f). n.s. = not significant. $p < 0.0001$: in **c**, $p = 5.99 \times 10^{-6}$, in **d**, $p = 3.64 \times 10^{-5}$, in **f** (left to right), $p = 1.11 \times 10^{-8}$, $p = 5.10 \times 10^{-8}$.

https://doi.org/10.1038/s41590-023-01691-y

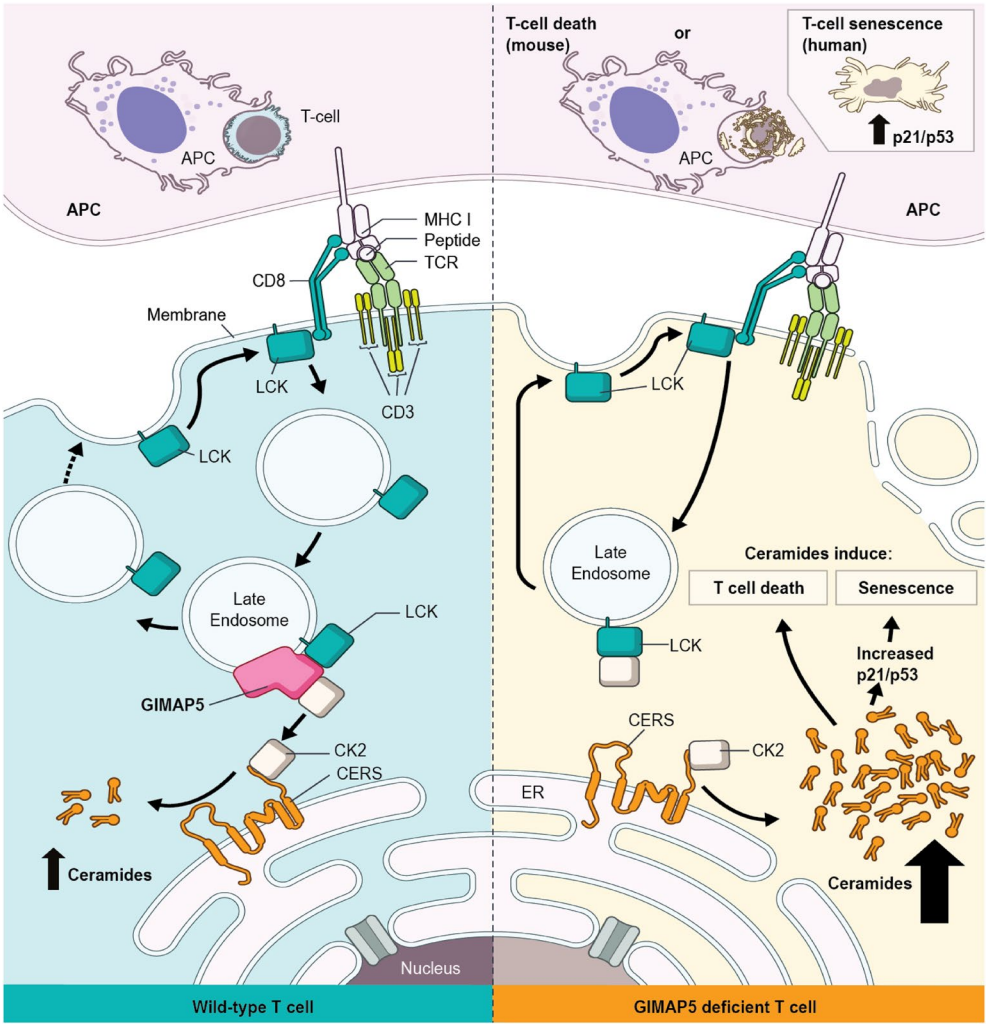


Extended Data Fig. 9 | See next page for caption.

https://doi.org/10.1038/s41590-023-01691-y

Extended Data Fig. 9 | Lack of senescence induction in T cells by C6-ceramide. **a-d**, Quantification of intracellular staining of SA-β-gal activity (CellEvent senescence green probe)(a, n = 3 per each group), p21 (b, day 3: n= 6, day 7: n = 3, day 10: n = 3), p53 (c, day 3: n = 6, day 7: n = 3, day 10: n = 3), and p16 (d, day 3: n= 6, day 7: n = 3, day 10: n = 3) in human T cell blasts with or without C6-Ceramide (C6-CER) treatment at days 3, 7, and 10 post-treatment. Mean and standard deviation of mean fluorescence intensity (MFI) is shown. **e**, Flow cytometry analysis of live/dead staining on human T cell blasts with or without C6-CER treatment for 3 days. **f**, Quantification of the live percentage by gating on the negative population of the live/dead staining as in (e). T cell blasts from healthy donors were treated for 3 days (n = 6), 7 days (n = 3), and 10 days (n = 3) at 0, 1, 3, and 10 mM (for 3 days) of C6-CER. All data are mean ± s.d. and were analyzed by two-tailed, unpaired Student's t-test (a-d, f). n.s. = not significant.

https://doi.org/10.1038/s41590-023-01691-y



Extended Data Fig. 10 | A model of GIMAP5 regulating CER levels through CK2 following TCR stimulation. Upon TCR stimulation, the interaction of GIMAP5, CK2, and LCK rapidly increases. CK2 then dissociates from GIMAP5 and LCK when LCK-containing endosomes are transported to the plasma membrane. Following dissociation from GIMAP5 and LCK, CK2 interacts with and activates CERS thereby generating CER following TCR stimulation (left). GIMAP5 deficiency in T cells results in constitutive and sustained CK2-CERS association leading to the accumulation of CER which induces T cell death or T cell senescence through the upregulation of p21 and p53 (right).

nature research

Corresponding author(s): Michael J. Lenardo

Last updated by author(s): Nov 26, 2023

Reporting Summary

Nature Research wishes to improve the reproducibility of the work that we publish. This form provides structure for consistency and transparency in reporting. For further information on Nature Research policies, see our Editorial Policies and the Editorial Policy Checklist.

Statistics

For all statistical analyses, confirm that the following items are present in the figure legend, table legend, main text, or Methods section.

n/a	Confirmed	
☐	☒	The exact sample size (*n*) for each experimental group/condition, given as a discrete number and unit of measurement
☐	☒	A statement on whether measurements were taken from distinct samples or whether the same sample was measured repeatedly
☐	☒	The statistical test(s) used AND whether they are one- or two-sided *Only common tests should be described solely by name; describe more complex techniques in the Methods section.*
☒	☐	A description of all covariates tested
☐	☒	A description of any assumptions or corrections, such as tests of normality and adjustment for multiple comparisons
☐	☒	A full description of the statistical parameters including central tendency (e.g. means) or other basic estimates (e.g. regression coefficient) AND variation (e.g. standard deviation) or associated estimates of uncertainty (e.g. confidence intervals)
☐	☒	For null hypothesis testing, the test statistic (e.g. *F*, *t*, *r*) with confidence intervals, effect sizes, degrees of freedom and *P* value noted *Give P values as exact values whenever suitable.*
☒	☐	For Bayesian analysis, information on the choice of priors and Markov chain Monte Carlo settings
☒	☐	For hierarchical and complex designs, identification of the appropriate level for tests and full reporting of outcomes
☐	☒	Estimates of effect sizes (e.g. Cohen's *d*, Pearson's *r*), indicating how they were calculated

Our web collection on statistics for biologists contains articles on many of the points above.

Software and code

Policy information about availability of computer code

Data collection	No Custom Code
Data analysis	Prism 8, Flowjo (V10.5.3, V10.8.0, V9.3, V10.6.2), SPADE v.3.9, Cytoscape3.8.2, MetaboAnalyst 3.0, MultiQuant® Software 3.0.3, MarkerView® Software 1.3.1, Agilent Mass Hunter software B.08.02, Imaris 9.2.1, R studio Version 4.0.0, ImageJ 1.53t, FACS Diva v9.3.1, Coot 0.7, Refmac5 5.2.0019, Molrep 9.0.09, PyMOL Version 1.7.6.2.

For manuscripts utilizing custom algorithms or software that are central to the research but not yet described in published literature, software must be made available to editors and reviewers. We strongly encourage code deposition in a community repository (e.g. GitHub). See the Nature Research guidelines for submitting code & software for further information.

Data

Policy information about availability of data

All manuscripts must include a data availability statement. This statement should provide the following information, where applicable:

- Accession codes, unique identifiers, or web links for publicly available datasets
- A list of figures that have associated raw data
- A description of any restrictions on data availability

The human exome and genome sequencing data reported in this paper will be deposited in dbGaP as phs002816.v1.p1. The coordinates and structure factors for the crystal structure have been deposited at the Protein Data Bank (PDB) with the accession code 6Z3E. Database/Datasets used: Protein Data Bank 2XTP, 2XTO, 3ZJC, 10X Genomics: 3k PBMCS from a healthy donor https://www.10xgenomics.com/resources/datasets/3-k-pbm-cs-from-a-healthy-donor-1-standard-1-1-0.

Field-specific reporting

Please select the one below that is the best fit for your research. If you are not sure, read the appropriate sections before making your selection.

☒ Life sciences ☐ Behavioural & social sciences ☐ Ecological, evolutionary & environmental sciences

For a reference copy of the document with all sections, see nature.com/documents/nr-reporting-summary-flat.pdf

Life sciences study design

All studies must disclose on these points even when the disclosure is negative.

Sample size	The sample size of 3-15 per group were used for in vitro and in vivo studies. These numbers were chosen based on hundreds of experiments (such as PMID: 32647003, PMID: 24165795, and PMID: 26206937) in our lab.
Data exclusions	No data were excluded.
Replication	All experiments presented in the manuscript were found to be reproducible through at least 2 independent experiments, often performed separately by independent members of the research team.
Randomization	Random allocation of WT and mutant mice in Fig.3 and Extended Data Fig. 3 and 4. For all other experiments, randomization was not done because experiments either compared subjects with and without the loss-of-function mutations, or sampled from a cell suspension for treatment/evaluation.
Blinding	Investigators were blinded wherever possible during sample analysis by coding sample identity during data collection for mice experiment and confocal experimentation (ie Fig.3, Extended Data Fig3, and 7). Else, blinding was not possible as the same investigator performed experiments and data analytics.

Reporting for specific materials, systems and methods

We require information from authors about some types of materials, experimental systems and methods used in many studies. Here, indicate whether each material, system or method listed is relevant to your study. If you are not sure if a list item applies to your research, read the appropriate section before selecting a response.

Materials & experimental systems

n/a	Involved in the study
☐	☒ Antibodies
☐	☒ Eukaryotic cell lines
☒	☐ Palaeontology and archaeology
☐	☒ Animals and other organisms
☐	☒ Human research participants
☐	☒ Clinical data
☒	☐ Dual use research of concern

Methods

n/a	Involved in the study
☒	☐ ChIP-seq
☐	☒ Flow cytometry
☒	☐ MRI-based neuroimaging

Antibodies

Antibodies used

Lot #s are provided where available.
Mouse monoclonal anti-CD3 (clone HIT3a), BioLegend, Cat# 300332, Lot# B217122
Mouse monoclonal anti-CD3 (clone UCHT1), BioLegend, Cat# 300438, Lot# B217470
Mouse monoclonal anti-CD28 (clone CD28.2), BioLegend, Cat# 302934
Rat anti-GIMAP1 (MAC451), Dr. Geoffrey Butcher
Rat anti-GIMAP4 (MAC426), Dr. Geoffrey Butcher
Rat anti-GIMAP5 (MAC429), Dr. Geoffrey Butcher
Rat anti-GIMAP6 (MAC445), Dr. Geoffrey Butcher
Rat anti-GIMAP7 (MAC453), Dr. Geoffrey Butcher
Rabbit anti-GIMAP2 (557/558), GenScript
Rabbit anti-GIMAP8 (597/589), GenScript
Rat anti-GIMAP5 (MAC421), Barnes et al.15
Rabbit polyclonal anti-GIMAP5, Cell Signaling Technology, Cat# 14108, Lot# 1
Mouse monoclonal anti-beta-Actin (clone mAbcam 8226), Abcam, Cat# ab20272
Rabbit monoclonal anti-HSP90 (C45G5), Cell Signaling Technology, Cat# 4877, Lot# 5
Rabbit monoclonal anti-p21 Waf1/Cip1 (12D1), Cell Signaling Technology, Cat# 2947, Lot# 12
Rabbit monoclonal anti-p21 Waf1/Cip1 (Mouse Preferred), Cell Signaling Technology, Cat# 64016, Lot# 1
Mouse monoclonal anti-p53 (clone DO-1), Sigma-Aldrich, Cat# MABE327, Lot# 3639361
Rabbit monoclonal anti-p16 INK4A (D7C1M) , Cell Signaling Technology, Cat# 80772, Lot# 3

Mouse monoclonal anti p16INK4a (1E12E10), Thermo Fisher Scientific, Cat# MA5-17142, Lot# XB3495823
Rabbit monoclonal anti-Phospho-p44/42 MAPK (Erk1/2) (Thr202/Tyr204) (D13.14.4E), Cell Signaling Technology, Cat# 4370, Lot# 24
Rabbit polyclonal anti-Phospho-p70 S6 Kinase (Thr421/Ser424), Cell signaling technology, Cat# 9204, Lot# 15
Rabbit polyclonal anti-c-Myc, Sigma-Aldrich, Cat# C3956
Mouse monoclonal anti-CK2 alpha (clone 844720), R&D systems, Cat# MAB7957, Lot# CHSNo 12306B
Rabbit polyclonal anti-CK2 alpha (CSNK2A1), Proteintech, Cat# 10992-1-AP, Lot# 00119842
Rabbit polyclonal anti-CK2 beta (CSNK2B), Proteintech, Cat# 22418-1-AP
Rabbit IgG-UNLB, SouthernBiotech, Cat# 0111-01, Lot# E4612-RD52
Rabbit polyclonal anti-Lass2 (Cers2), Thermo Fisher Scientific, Cat# PA5-55560, Lot# YG3986771A
Mouse monoclonal anti-Lck (L22B1), Cell Signaling Technology, Cat#: 2657, Lot# 4
Mouse monoclonal anti-Lck (clone A17013D), BioLegend, Cat# 601002, Lot# B252787
Mouse monoclonal anti-GFP (4B10), Cell Signaling Technology, Cat# 2955, Lot# 2
Rabbit monoclonal anti-LAMP1 (D2D11), Cell Signaling Technology, Cat# 9091, Lot# 1
Rabbit monoclonal anti-Rab7 (D95F2), Cell Signaling Technology, Cat# 9367, Lot# 1
Rabbit monoclonal anti-LAMTOR4 (D4P6O), Cell Signaling Technology, Cat# 13140, Lot# 1
Rat monoclonal anti-Calnexin (clone W17077C), BioLegend, Cat# 699402, Lot# B319774
Goat anti-Rabbit IgG (H+L) Secondary Antibody, Alexa Fluor™ Plus 647, Thermo Fisher Scientific, Cat# A32733, Lot# TB264033
Goat anti-Rat IgG (H+L) Secondary Antibody, Alexa Fluor™ 647, Cat# A2247, Lot# 1182663
Goat anti-Mouse IgG (H+L) Secondary Antibody, Alexa Fluor™ 488, Cat# A11029, Lot# 2486523
Goat anti-Rabbit IgG (H+L) Secondary Antibody, Alexa Fluor™ Plus 555, Cat# A32732, Lot# TB244421
Goat anti-Mouse IgG (H+L) Secondary Antibody, Alexa Fluor™ Plus 555, Cat# A32727, Lot# TA252658
Donkey anti-Rat IgG (H+L) Secondary Antibody, Alexa Fluor™ 488, Cat# A21208, Lot# 1979698
Goat anti-Rabbit IgG (H+L) Secondary Antibody, Alexa Fluor™ Plus 488, Cat# A32731, Lot# WF322198
PE Mouse monoclonal anti-CD3 (HIT3a), BioLegend, Cat# 300308, Lot# B326668
APC/Cyanine7 Mouse monoclonal anti-human CD4 (clone RPA-T4), BioLegend, Cat# 300518, Lot# B384817
PE/Cyanine7 Mouse monoclonal anti-human CD8 (clone RPA-T8), BioLegend, Cat# 301012, Lot# B346118
APC Mouse monoclonal anti-human CD197 (CCR7) (clone G043H7), BioLegend, Cat# 353214
FITC Mouse monoclonal anti-human CD45RA (clone HI100) , BioLegend, Cat# 304106, Lot# B274083
PE Mouse monoclonal anti-human CD57 antibody (clone HNK-1), BioLegend, Cat# 359612, Lot# B337046
APC Mouse monoclonal anti-human CD25 (clone M-A251), BioLegend, Cat# 356110, Lot# B349603
FITC Mouse monoclonal anti-human CD69 (clone FN50), BioLegend, Cat# 310904, Lot# B347085
APC Syrian Hamster monoclonal anti-mouse/human KLRG1 (clone 2F1/KLRG1), BioLegend, Cat# 138412, Lot# B344824
Pacific Blue™ Mouse monoclonal anti-human CD27 (clone M-T271), BioLegend, Cat# 356414, Lot# B332973
FITC Mouse monoclonal anti-human CD28, BioLegend (CD28.2), Cat# 302906, Lot# B255054
Brilliant Violet 421™ Mouse monoclonal anti-human CD279 (PD-1) Antibody (clone EH12.2H7), BioLegend, Cat# 329920, Lot# B336297
Rabbit monoclonal p21 Waf1/Cip1 (12D1) (Alexa Fluor® 488 Conjugate), Cell Signaling Technology , Cat# 5487, Lot# 11
Alexa Fluor® 594 Mouse monoclonal anti-p53 Antibody (clone DO-1), BioLegend, Cat# 645706, Lot# B399393
p16 INK4A (D7C1M) Rabbit mAb (Alexa Fluor® 647 Conjugate) , Cell Signaling Technology , Cat# 43161, Lot# 2
Alexa Fluor 647 Rabbit monoclonal anti-Mouse p21 (clone EPR18021), Abcam, Cat# ab237265, Lot# GR3419425-1
FITC Mouse monoclonal anti-p53 Set (clone G59-12), BD Biosciences, Cat# 557026, Lot# 2115419
APC anti-mouse CD4 Antibody (clone GK1.5) , BioLegend, Cat# 100411, Lot# E07037-1633
PE Mouse monoclonal anti-mouse CD8a (clone 53-6.7), BioLegend, Cat# 100708, Lot# B361028
FITC Rat monoclonal anti-mouse/human CD44 (clone IM7), BioLegend , Cat# 103006, Lot# B156153
APC Rat monoclonal anti-mouse CD62L (clone MEL-14), BioLegend , Cat# 104412, Lot# B170234
Brilliant Violet 421™ anti-mouse CD31 (clone 390), BioLegend , Cat# 102424, Lot# B347936
PE/Cyanine7 Mouse recombinant anti-CD45 (clone QA17A26), BioLegend , Cat# 157614, Lot# B307109
PE anti-rat CD90/mouse CD90.1 (Thy-1.1) (clone OX-7) , BioLegend, Cat# 202524, Lot# B160926
Purified Rat monoclonal anti-DYKDDDDK Tag (FLAG tag) (clone L5), BioLegend, Cat# 637303, Lot# B332382
Rabbit monoclonal anti-FLAG Tag, Cell Signaling Technology (D6W5B), Cat# 14793, Lot# 7
Rabbit monoclonal anti-HA-tag , Cell Signaling Technology (C29F4), Cat# 3724, Lot# 10
Rabbit polyclonal anti-beta-Tubulin, Cell Signaling Technology, Cat# 2146
F(ab')2 Fragment Goat Anti-Mouse IgG, Jackson Immunoresearch, Cat# 115-006-006, Lot# 163193

Validation

Validation for GIMAP5 MAC421: PMID 20190135, GIMAP5 429: PMID 21487483421, GIMAP6 MAC445: PMID 24204963, GIMAP1 MAC451, GIMAP7 MAC453, and GIMAP2: In-house validation by CRISPR-Cas9 knockout followed by western blotting, GIMAP8: In-house validation through western blotting and molecular weight comparison. Antibodies from Biolegend, Cell Signaling Technology, Abcam, Sigma-Aldrich, Thermo Fisher Scientific, R&D Systems, Proteintech, and BD Biosciences were validated by the suppliers using various supplier-specific methodologies.

Eukaryotic cell lines

Policy information about cell lines

Cell line source(s)

HEK293T (CRL-3216), NIH3T3 (CRL-1658), and Jurkat (TIB-152) cells were purchased from ATCC. Platinum-E (RV-101) cells were purchased from Cell Biolabs. Lenti-X (632180) cells were purchased from Takara.

Authentication

Cell lines were authenticated by the suppliers, not in-house.

Mycoplasma contamination

The cell lines were not tested for mycoplasma concentration.

Commonly misidentified lines
(See ICLAC register)

No commonly misidentified cell line used.

Animals and other organisms

Policy information about studies involving animals; ARRIVE guidelines recommended for reporting animal research

Laboratory animals	Gender-matched 4- to 12-week-old C57BL/6 and 4- to 12-week old sphinx mice (Gimap5sph/sph) or old (16- to 19-month-old) mice were used for all experiments. Animal rooms are maintained at 21 degrees with 30-70% humidity and 12 hour dark/light cycle.
Wild animals	This study did not involve wild animals.
Field-collected samples	This study did not involve field-collected samples.
Ethics oversight	Animal procedures were performed under protocols approved by the NIAID Animal Care and Use Committee.

Note that full information on the approval of the study protocol must also be provided in the manuscript.

Human research participants

Policy information about studies involving human research participants

Population characteristics	Individual patient characteristics described in the manuscript; main text, Figure 1, Extended Data Figure 1, Supplementary Data Table 1 and 2, and Supplementary Clinical Descriptions.
Recruitment	All patients were recruited to a genomics study during treatment for an immune disorder. Since we describe a rare monogenic disease, selection bias is not relevant.
Ethics oversight	All enrolled subjects provided written informed consent and were collected through protocols following local ethics and IRB recommendations. Local ethics boards involved: Ankara University Faculty of Medicine Clinical Research Ethics Committee, Gazi University Ethics Committee, Hacettepe University Clinical Trials Ethics Committee, Marmara University Research Ethics Committee.

Note that full information on the approval of the study protocol must also be provided in the manuscript.

Clinical data

Policy information about clinical studies

All manuscripts should comply with the ICMJE guidelines for publication of clinical research and a completed CONSORT checklist must be included with all submissions.

Clinical trial registration	Patients P1.1-P1.6, and patient P4.1 were enrolled on NCT00246857. Patients P2.1-P2.2 were enrolled by Ankara University Faculty of Medicine Clinical Research Ethics Committee. Patients P3.1-P.3.2 were enrolled by protocol approved by Gazi University Ethics Committee. Patient P5.1 was enrolled on NCT000011350. Patient P6.1 was enrolled on NCT00001355. Patient 7.1 was enrolled by Hacettepe University Clinical Trials Ethics Committee, Decision No.: 2019/21-36. Patients P8.1 and P9.1 were approved by T.C. Marmara University Research Ethics Committee Document id: 70737436-050.01.04-E.2000065366.
Study protocol	Study protocols are provided in the manuscript (method section).
Data collection	Blood samples were collected from enrolled patients and patient relatives at their local healthcare facility. Recruitment is ongoing and the study plans to enroll up to 5000 participants over the next 20 years. Per protocol, data is collected at least once within a year of enrollment. All data and samples were collected following local ethics and IRB policies.
Outcomes	"Outcomes" is not applicable for this study as it is centered around data collection and study rather than treatment.

Flow Cytometry

Plots

Confirm that:

☒ The axis labels state the marker and fluorochrome used (e.g. CD4-FITC).

☒ The axis scales are clearly visible. Include numbers along axes only for bottom left plot of group (a 'group' is an analysis of identical markers).

☒ All plots are contour plots with outliers or pseudocolor plots.

☒ A numerical value for number of cells or percentage (with statistics) is provided.

Methodology

Sample preparation	For surface staining, PBMCs and T cell blasts were washed in fluorescence activated cell sorting (FACS) buffer (PBS containing 5% FBS and 0.1% NaN3) and stained in FACS buffer containing indicated fluorochrome-labeled antibodies for 30 mins on ice. Cells were then washed three times in FACS buffer and fixed before acquisition. For viability analyses, PBMCs and T cell blasts were stained with Zombie Aqua™ viability dye (BioLegend). For intracellular staining, cells were fixed and permeabilized with BD Cytofix/Cytoperm™ solution for 20 mins at 4ºC and then washed twice in BD Perm/Wash™ buffer. Cells were then

	incubated in BD Perm/Wash™ buffer containing fluorochrome-conjugated antibodies for 30 mins at 4 ºC in the dark. Cells were washed twice with BD Perm/Wash™ buffer, once with FACS buffer, and resuspended in FACS buffer before acquisition. For mouse p21 staining, cells were fixed with 80% methanol for 5 mins and permeabilized with 0.1% Triton X-100 in PBS for 15 mins. Cells were then blocked with 10% goat serum in 1x PBS for 30 mins and incubated with Alexa Fluor 647 Anti-p21 antibody (Abcam) for 30 mins at RT. Cells were washed three times in FACS buffer before acquisition.
Instrument	BD Fortessa, BD LSR II, BD FACSymphony
Software	FACS Diva and FlowJo
Cell population abundance	We did not use sorting and thus cell population abundance is not relevant to the study.
Gating strategy	Lymphocytes and endothelial cells were gated using FSC vs SSC, and singlets were selected. The appropriate cell type was gated and indicated markers were assessed. Gates were set on control samples to enable clear separation between populations and gates were kept constant across comparison samples.

☒ Tick this box to confirm that a figure exemplifying the gating strategy is provided in the Supplementary Information.